Experimental constraints on Li isotope fractionation during clay formation

Ruth S. Hindshaw[a,*], Rebecca Tosca[b], Thomas L. Goût[a], Ian Farnan[a], Nicholas J. Tosca[b], Edward T. Tipper[a]

[a]*Department of Earth Sciences, University of Cambridge, Downing Street, Cambridge, UK, CB2 3EQ*
[b]*Department of Earth Sciences, University of Oxford, South Parks Road, Oxford, UK, OX1 3AN*

Abstract

Knowledge of the lithium (Li) isotope fractionation factor during clay mineral formation is a key parameter for Earth system models. This study refines our understanding of isotope fractionation during clay formation with essential implications for the interpretation of field data and the global geochemical cycle of Li. We synthesised Mg-rich layer silicates (stevensite and saponite) at temperatures relevant for Earth surface processes. The resultant solids were characterised by X-ray diffraction (XRD) and Fourier-transform infrared spectroscopy (FT-IR) to confirm the mineralogy and crystallinity of the product.

Bulk solid samples were treated with ammonium chloride to remove exchangeable Li in order to distinguish the Li isotopic fractionation between these sites and structural (octahedral) sites. Bulk solids, residual solids and exchangeable solutions were all enriched in ^{6}Li compared to the initial solution. On average, the exchangeable solutions had δ^7Li values 7‰ lower than the initial solution. The average difference between the residue and initial solution δ^7Li values (Δ^7Li$_{residue-solution}$) for the synthesised layer silicates was -16.6±1.7‰ at 20°C, in agreement with modelling studies, extrapolations from high temperature experimental data and field observations. Three bonding environments were identified from ^{7}Li-NMR spectra which were present in both bulk and residual solid ^{7}Li-NMR spectra, implying that some exchangeable Li remains after treatment with ammonium chloride. The ^{7}Li-NMR peaks were assigned to octahedral, outer-sphere (interlayer and adsorbed) and pseudo-hexagonal (ditrigonal cavity) Li. By combining the ^{7}Li-NMR data with mass balance constraints we calculated a fractionation factor, based on a Monte Carlo minimum misfit method, for each bonding environment. The calculated values are -21.5±1.1‰, -0.2±1.9‰ and 15.0±12.3‰ for the octahedral, outer-sphere and pseudo-hexagonal sites respectively (errors 1σ). The bulk fractionation factor (Δ^7Li$_{bulk-solution}$) is dependent on the chemistry of the initial solution. The higher the Na concentration in the initial solution the lower the bulk δ^7Li value. We suggest this is due to Na outcompeting Li for interlayer sites and as interlayer Li has a high δ^7Li value relative to octahedral Li, increased Na serves to lower the bulk δ^7Li value. Three experiments conducted at higher pH exhibited lower δ^7Li values in the residual solid. This could either be a kinetic effect, resulting from the higher reaction rate at high pH, or an equilibrium effect resulting from reduced Li incorporation in the residual solid and/or a change in Li speciation in solution.

This study highlights the power of ^{7}Li-NMR in experimental studies of clay synthesis to target site specific Li isotope fractionation factors which can then be used to provide much needed constraints on field processes.

Keywords: Li isotopes, Clay minerals, Clay synthesis, Biogeochemical cycles

1. Introduction

Lithium (Li) is a trace element which is predominantly found in silicate minerals (e.g. Tardy et al., 1972; Huh et al., 1998). Li has two stable isotopes, [6]Li and [7]Li, and variations in their relative abundance are expressed in standard delta notation as δ^7Li. The natural range of δ^7Li in geological and environmental materials is approximately 60‰ (Tomascak, 2004), with much of this range thought to be generated by fractionation associated with the preferential incorporation of [6]Li into clay minerals and adsorption/exchange onto particle surfaces (e.g. Zhang et al., 1998; Vigier et al., 2008). No appreciable amount of Li is incorporated into the biosphere and fractionation of Li by plants is thought to be negligible (Lemarchand et al., 2010; Clergue et al., 2015). There is no appreciable fractionation of Li isotopes during mineral dissolution at low temperatures <50 °C (Pistiner and Henderson, 2003; Wimpenny et al., 2010a; Verney-Carron et al., 2011). For these reasons, Li isotopes are one of the most promising tracers to emerge in recent decades for the intensity of silicate weathering; defined as the ratio of the total erosion mass flux to the total weathering mass flux (Bouchez et al., 2013). Records of δ^7Li in marine carbonates, interpreted to be representative of seawater δ^7Li over the Phanerozoic, potentially provide a unique record of changing silicate weathering intensity over time, with implications for the importance of weathering-related feedbacks in the long-term carbon cycle (Froelich and Misra, 2014; Vigier and Goddéris, 2015; Pogge von Strandmann et al., 2017a). The seawater Li isotope record (Hall et al., 2005; Hathorne and James, 2006; Misra and Froelich, 2012; Pogge von Strandmann et al., 2013; Lechler et al., 2015; Pogge von Strandmann et al., 2017a) has been interpreted to reflect 1) variations in the mean riverine δ^7Li flux and thus changes in continental silicate weathering processes through time (Hathorne and James, 2006; Misra and Froelich, 2012; Wanner et al., 2014; Vigier and Goddéris, 2015; Pogge von Strandmann et al., 2017a), 2) a change in the balance between low and high temperature sinks of Li from the oceans (Li and West, 2014) and 3) changes in the balance between continental and submarine basalt weathering (for Jurassic ocean anoxic events, Lechler et al., 2015; Pogge von Strandmann et al., 2017a). The mass balance of Li in seawater is controlled by inputs from continental weathering and marine hydrothermal systems, and outputs due to removal by clays (alteration of oceanic crust and reverse weathering). Critically, both the inputs and outputs of Li are affected by Li isotope fractionation associated with the formation of secondary phases (clays) but the magnitude of fractionation lacks experimental constraints, particularly at temperatures relevant to weathering and reverse weathering (<50°C). To date, different studies have assumed different fractionation factors ranging from 13 to 30‰ (Hathorne and James, 2006; Misra and Froelich, 2012; Li and West, 2014; Wanner et al., 2014), which have been compiled/extrapolated from field studies and a limited number of experimental studies (Vigier et al., 2008).

Li isotope fractionation attendant to clay mineral formation likely occurs for a number of reasons. Firstly, Li may be incorporated into octahedral sites within the clay mineral structure. If isotopic equilibrium is attained, the

*corresponding author
Email address: ruth.hindshaw@gmail.com (Ruth S. Hindshaw)

magnitude of fractionation should depend on the vibrational frequency or bond strength between Li in octahedral sites and Li in solution (Bigeleisen, 1965). If the isotopic fractionation is kinetic then there may be an additional rate dependence (Schauble, 2004). Secondly, Li may be adsorbed to clay mineral surfaces, held on negatively charged layer surfaces, or be located in pseudo-hexagonal sites within the clay tetrahedral layer. These sites may fractionate Li isotopes if there are differences in bond strength (Pistiner and Henderson, 2003). The bulk fractionation factor in a clay therefore reflects the sum total of the isotope fractionation associated with each bonding environment.

Only one study to date has directly synthesised a clay mineral at low (Earth surface) temperature (hectorite, a Li-rich smectite, Vigier et al., 2008). Two studies have investigated incorporation of Li into existing mineral structures. The first investigated the uptake of Li during illitization (Williams and Hervig, 2005) and the second, the intercalation of Li into gibbsite (Wimpenny et al., 2015). Additionally, Li isotope fractionation has been observed during the formation of a solid inferred to be chrysotile as a by-product of forsterite dissolution at high pH (Wimpenny et al., 2010a) and during the formation of a mixture of smectite phases (nontronite, beidellite) resulting from basalt-seawater interaction experiments (Millot et al., 2010b). High-temperature and pressure experiments have investigated Li isotope fractionation during mineral (mica, staurolite, spodumene, serpentine-group) formation (Wunder et al., 2006, 2007, 2010) and Li assimilation (Lynton et al., 2005).

Adsorption of Li onto several types of mineral (zeolite, vermiculite, kaolinite, smectite, ferrihydrite, gibbsite) has been reported (Taylor and Urey, 1938; Zhang et al., 1998; Pistiner and Henderson, 2003) together with indirect measurements of adsorption onto vernadite and amorphous Fe oxides from Li isotope measurements of bulk Fe-Mn crusts (Chan and Hein, 2007). The resultant fractionation is interpreted to depend on the strength of the Li-surface bond i.e. whether an inner or an outer-sphere complex is formed, with the more strongly-bound inner-sphere complexes resulting in greater Li isotope fractionation relative to the starting solution (Pistiner and Henderson, 2003). In all studies of adsorbed and structurally incorporated Li, ^{6}Li was preferentially incorporated, consistent with results from density functional theory models which predict that ^{7}Li is preferentially retained in the aquo-complex (Yamaji et al., 2001; Bogatko et al., 2013).

Some studies have explicitly tried to focus on octahedral (structural) Li by treating the solids to remove exchange-able Li and then measuring the Li isotopic composition of the residue (Williams and Hervig, 2005; Vigier et al., 2008), whereas others refer to a bulk phase including octahedral and exchangeable Li (Wimpenny et al., 2015). The term 'exchangeable' is used to encompass all the Li held in loosely bound sites, for example, in the interlayer or adsorbed to negatively charged layer surfaces. It has been suggested that Li held in outer-sphere bonding sites, which is thought to be the case for Li adsorbed to smectites and interlayer Li, is not isotopically fractionated relative to the solution (Pistiner and Henderson, 2003; Chan and Hein, 2007). This implies that bulk phases including a fraction of exchangeable Li will have δ^7Li values closer to the initial solution than those where all the exchangeable Li has been removed (Wimpenny et al., 2015).

All experimental data considered to be free of non-equilibrium effects were found to be in good agreement with theoretical modelling predictions (Dupuis et al., 2017). In agreement with equilibrium fractionation, increasing the

temperature decreased the fractionation factor during hectorite formation (Vigier et al., 2008). In contrast, during chrysotile precipitation, the higher temperature experiments led to a greater difference in δ^7Li between the solid formed and the final solution composition (Wimpenny et al., 2010a). Vigier et al. (2008) found that the measured fractionation factor did not depend on the amount of Li incorporated into hectorite or the solution composition whereas Wimpenny et al. (2015) found that fractionation of Li during intercalation of Li into gibbsite was dependent on the availability of free octahedral sites and the identity of anions in solution. Neither the structure nor composition of the clay formed influenced the magnitude of Li isotope fractionation into phyllosilicates (Dupuis et al., 2017). Further studies have investigated the effect of physical controls such as crystal size on the magnitude of fractionation (Williams and Hervig, 2005; Wunder et al., 2010).

Collectively, these studies have found that the extent of Li isotope fractionation depends on 1) coordination number (bond strength), 2) temperature and 3) chemistry of solution, including pH. Similar controls on stable isotope fractionation have been inferred for other elements (e.g. Tang et al., 2008; Nielsen et al., 2012; Li et al., 2014). Most previous experimental studies have focussed on high temperature synthesis methods as these typically involve higher crystallisation rates which, in turn, generate larger amounts of crystalline material over shorter experimental timescales (Tosca and Masterson, 2014). However, whether these data are reflective of secondary mineral formation at Earth surface temperatures is less clear. In this study, we apply a low temperature synthesis method to synthesise smectite-group minerals directly from solution and investigate the controls on the resultant Li isotope fractionation. Further, we use a cation exchange procedure to distinguish exchangeable from octahedral Li coupled with ^{7}Li-NMR to quantify the fraction of Li in each bonding environment, permitting us to estimate site specific fractionation factors.

1.1. Mg-rich layer silicate minerals

We precipitated two layer silicate structures directly from solution: stevensite and saponite. These belong to the Mg-smectite group of minerals $((Na,Ca)_{0.3}(Al,Mg)_2Si_4O_{10}(OH)_2 \cdot nH_2O)$ comprised of layers of octahedra (Mg or Al bonded to O or OH) sandwiched between two layers of Si tetrahedra (Si bonded to O or OH, Fig. 1), thus this structure is also referred to as 'TOT' or '2:1 layer'. Smectites are found in numerous low temperature environments (marine and continental) and as such they constitute an important reservoir of Mg; a major element which can readily transfer between the crust, mantle and hydrosphere. Li, on the other hand, is a trace element but due the similar ionic radii of Li and Mg, Li can readily substitute for Mg in minerals (Huh et al., 1998; Decarreau et al., 2012) and therefore Li may be able to help constrain the Mg biogeochemical cycle.

Stevensite is a trioctahedral layer silicate mineral with a Mg-rich octahedral sheet, a pure Si-rich tetrahedral sheet and octahedral vacancies (Guggenheim, 2016). In stevensite, the spacing between each TOT layer (d_{001}, Fig. 1) is ~14-15 Å depending on whether the sample is in the air-dried, hydrated or ethylene glycol-solvated state. Stevensite can only accommodate trace aluminium in the lattice (Guggenheim, 2016). The octahedral vacancies (~0.08-0.10 cation sites per unit) are thought to give rise to an overall layer charge which imparts swelling characteristics and interlayer ion accommodation similar to other members of the smectite group (Brindley et al., 1977; Steudel et al.,
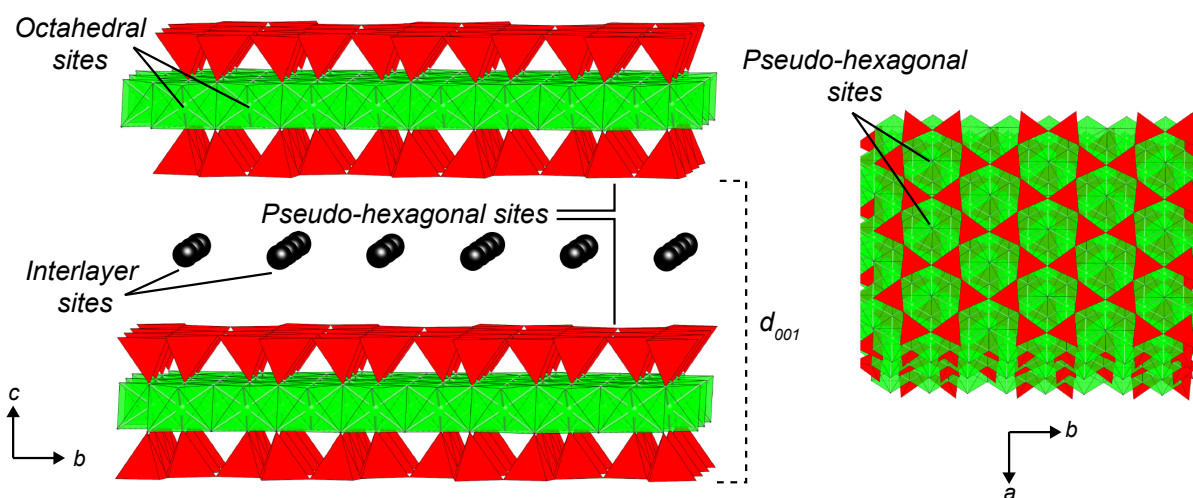
4

Figure 1: Schematic figure of the overall structure of a 2:1 layer silicate mineral shown from two different perspectives. Each layer consists of an octahedral sheet (green squares) sandwiched between two tetrahedral sheets (red triangles). In between, depending on the basal spacing (d_{001}), which is also related to the overall layer charge and therefore chemical composition of the octahedral sheet, there can be interlayer cations (depicted here without their hydration spheres). Three main crystallographic sites for Li are highlighted: octahedral, interlayer and pseudo-hexagonal sites. Li may also be adsorbed onto edge sites but this process is not depicted in this figure.

2017). Li can fill these octahedral vacancies and also substitute for Mg. A Mg-rich trioctahedral layer silicate closely related to stevensite is kerolite ($Mg_3Si_4O_{10}(OH)_2$).nH_2O; $n = 0.8$-1.2). Kerolite is non-expandable and is characterised by H_2O positioned either on edges associated with broken bonds or within the interlayer (Guggenheim, 2016). Kerolite exhibits a basal spacing commonly measured by powder X-ray diffraction (uncorrected for polarisation effects) of ~10.1 Å. Naturally occurring stevensite has been found to contain random mixed layers of kerolite, and the converse has also been observed (Eberl et al., 1982; Martin de Vidales et al., 1991; Dekov et al., 2008). Thus, as a result of their closely related structures and thermodynamic stability, kerolite and stevensite often occur together as direct precipitates from the weathering of ultramafic lithologies and from alkaline saline lakes (Stoessell and Hay, 1978; Jones, 1986; Tosca, 2016). Saponite is structurally similar to stevensite except Al^{3+} substitution for Si^{4+} in tetrahedral sites is more extensive. A trioctahedral smectite where Li and Mg occur as a major elements (wt%) is called hectorite. Stevensite, kerolite and saponite may all contain minor or trace amounts of Li in their structure and there is no formal division in terms of Li concentration between these structures and hectorite.

The Mg-rich trioctahedral layer silicate minerals offer an ideal starting point for investigating low temperature clay mineral precipitation because they exhibit relatively rapid reaction kinetics yet contain all of the essential structural characteristics of smectite and other TOT clay minerals.

2. Methods

2.1. Mg-rich layer silicate synthesis

There are established methods for both the high and low temperature synthesis of smectite clay minerals (e.g. Harder, 1972; Vogels et al., 2005). High temperature methods start with a seed or a gel which is then heated at temperatures >90°C (e.g. Güven and Carney, 1979; Vogels et al., 2005; Vigier et al., 2008). This method results in highly crystalline materials which are arguably most analogous to clays formed in hydrothermal settings. In contrast, low temperature methods rely on direct precipitation from solution (e.g. Harder, 1972; Tosca and Masterson, 2014). Although the quantity of solid formed is lower and the products are less crystalline than the products obtained from high temperature experiments, the experimental conditions of low temperature synthesis are arguably most representative of the majority of low temperature weathering environments (e.g. soils) and processes (e.g. diagenesis). These experiments may also be representative of what is occurring in early stage weathering environments where clay phases are often not detected but their presence is inferred from isotope fractionation (Tipper et al., 2012). Low temperature experiments are essential for directly determining fractionation factors at similar temperatures to the natural weathering environment, avoiding uncertainty associated with extrapolation from high temperature experiments.

We synthesised two different Mg-rich layer silicate minerals (stevensite and saponite) at room temperature (20°C) using two different methods. The first method used 1 L PPE bottles with an electrolyte buffer and the second method used a reaction vessel coupled to an autotitrator. These two setups are hereafter referred to as 'bottle' and 'reaction vessel' experiments.

For stevensite bottle experiments, the solutions contained Mg (from $MgCl_2$), Li (from LiCl), Na (from NaCl) and Si (from Na_2SiO_3) and the pH was adjusted to the required value using HCl and buffered for the duration of the experiment using TRIS (tris(hydroxymethyl)aminomethane). All experiments were stirred magnetically and the duration of the experiments varied from 9 days ('010217' series) to 28 days ('240417' series). For the saponite bottle experiment, the initial solution additionally contained Al (from $Al(NO_3)_3.9H_2O$) and was prepared similarly to those for stevensite except that the source of Si was TEOS (tetraethyl orthosilicate), which was allowed to dissociate for 24 h before Al and Mg were added to the solution. The solution also contained Ca (from $CaCl_2$) and the bottle was placed on a shaker table for 26 days. The stevensite reaction vessel experiment was conducted in a 1 L polycarbonate reaction vessel and used the same reagents as the stevensite bottle experiments but as the experiment was connected to an autotitrator which delivered 0.1 mol/kg NaOH, no buffer was needed. This experiment lasted for 14 days. The target initial concentrations of Si, Al, Mg, Na, Ca and Li used in the different experiments are listed in Table 1. A solid precipitate was recovered from all experiments apart from two experiments run at pH < 9.3 and low [Mg]. The pH of the experiments varied from 9.0 to 10.4 (Table 1). In general, the higher the pH, the greater the mass of the recovered precipitate for experiments of the same duration.

The elevated pH associated with the onset of nucleation and growth of Mg-rich layer silicate phases stems from the hydration characteristics of the Mg^{2+} ion. Nevertheless, the nucleation and growth processes involved in direct

Table 1: Summary of the target initial solution conditions for the stevensite and saponite synthesis experiments.

Experiment(s)	Type	Clay	pH	Temp °C	[Si] mmol/kg	[Al] mmol/kg	[Na] mmol/kg	[Mg] mmol/kg	[Li] mmol/kg	[Ca] mmol/kg
250117	Rxn vessel	stevensite	10.3	20	2.6	0	5	2	2	0
010217-E	bottle	stevensite	10.0	20	1.7	0	100	2	2	0
010217-F	bottle	stevensite	10.3	20	2.6	0	100	2	2	0
240417A-D, I, J	bottle	stevensite	9.0-10.2	20	2.2	0	500	2	2	0
240417E-H,K,L	bottle	stevensite	9.0-10.4	20	2.2	0	500	20	2	0
20140624F	bottle	saponite	9.5	20	3.7	0.07	1	33	1.2	0.5

precipitation of these phases from solution is thought to closely mirror other clay mineral systems containing, for example, Fe and Al (Tutolo and Tosca, 2018; Tosca, 2016). Alkaline pH is common in environments such as marine pore-waters, subglacial meltwaters and rivers draining basalt (Dessert et al., 2001; Gíslason et al., 1996; Reimers et al., 1996; Pokrovsky et al., 2005; Hindshaw et al., 2014). The canonical natural analogue for reverse weathering is African alkaline soda lakes (pH>9) where smectite-group minerals precipitate (Von Damm and Edmond, 1984). Although the pH of river water and bulk soil pore waters is generally close to neutral (Stumm and Morgan, 1996), the pH of soil pore waters at the nano- to micro-scale, where coupled mineral dissolution and precipitation reactions occur, is higher than that measured in bulk soil solutions (Hochella and Banfield, 1995; Carrado et al., 2006). Therefore the experimental conditions are a good analogue for many, but not all, natural settings.

Aliquots (2 mL) of the initial and final solution were collected from all experiments and filtered at 0.22 μm. Solids from all experiments were recovered by filtration through 0.1 μm nitrocellulose filters. The solid was air-dried and saved for analysis.

Part of the recovered clay sample was saturated with 1 M NH_4Cl in order to extract the Li bound in exchangeable sites (Vigier et al., 2008). 10 mg of the clay was placed in a 2 mL centrifuge tube with 1 mL 1 M NH_4Cl. The mixture was shaken overnight, centrifuged and the supernatant pipetted off. This procedure was performed in triplicate for experiment 20140624F and once for all other experiments. The supernatant was dried down and digested in concentrated HNO_3. The residue and an untreated bulk aliquot were digested in a mixture of concentrated HF and HNO_3 and then repeatedly dried down and redissolved in 6 M HCl. Once digested, the samples were dissolved in 2% HNO_3 in preparation for concentration analysis.

2.2. Concentration and Li isotope measurements

All Li and Mg concentrations were measured by inductively-coupled plasma optical emission spectrometry (ICP-OES, Agilent Technologies 5100, University of Cambridge) in cool plasma mode to ensure a low Li background and using matrix matched standards. The RSD of water standard TM25.4 (Environment Canada) was 3.2%. Concentrations of the residual and exchangeable fractions are given as mg Li per kg of bulk sample. Li isotopes were measured using a procedure described in Hindshaw et al. (2018). Briefly, a sample containing 15-20 ng Li was dried down and passed through a column containing 3 mL Bio-Rad AG 50W-X12 200-400 mesh resin, eluting with 0.2 M HCl. Lithium isotope ratios were measured on a Neptune Plus multi-collector ICP-MS using an APEX IR sample intro-

duction system, a 50 μL/min PFA nebuliser and nickel H cones. ^{7}Li/^{6}Li ratios were normalised to L-SVEC (NIST RM 8545) using standard-sample bracketing. Analyses were performed on 5 ppb solutions using a 10^{13} Ω resistor on the pre-amplifier for ^{6}Li (Bohlin et al., 2018). The typical beam-size for samples was around 1 V on ^{7}Li and the background was typically between 5 and 20 mV. Accuracy and precision were monitored using Li6-N and Li7-N solutions which gave values of -8.1±0.9‰ (2SD, n=59) and +30.2±0.9‰ (2SD, n=50) respectively. These values are in agreement with previously published values for these standards (Li7-N = +30.2‰ and Li6-N = -8.2‰, Carignan et al., 2007; Millot et al., 2010c). Long-term reproducibility of L-SVEC was +0.1±0.5‰ (2SD, n=72). To ensure there was no fractionation induced during chemical separation, either seawater or a rock standard was processed with every batch of 5 samples. Long-term reproducibility for seawater (OSIL IAPSO batch P157) is +30.8±1.1‰ (2SD, n=45) in agreement with the compiled values of +31.1‰ (Carignan et al., 2004) and +30.8 ‰ (Rosner et al., 2007). We obtained a value of +4.9±1.9‰ (2SD, n = 10) for USGS shale rock standard SGR-1b (Hindshaw et al., 2018), in agreement with previously published values (Phan et al., 2016; Pogge von Strandmann et al., 2017b; Bohlin et al., 2018). The long-term external reproducibility of seawater is applied to the samples measured in this study (1.1‰), as this value is greater than the 2SD of individual sample measurements.

Table 2: Li concentration and isotope measurements of the analysed solids and solutions. Concentrations of the residual and exchangeable fractions are given as mg Li per kg of bulk sample.

Experiment	pH	solid g	[Li]i mg/L	δ^7Li$_i$[1] ‰	[Li]f mg/L	δ^7Li$_f$[1] ‰	[Li]e mg/kg	δ^7Li$_e$[1] ‰	[Mg]r g/kg	[Li]r mg/kg	δ^7Li$_r$[1] ‰	fe	fr	[Li]b mg/kg	[Li]b* mg/kg	δ^7Li$_b$[1] ‰	δ^7Li$_b$*[1] ‰	Δ^7Li$_{residue-init.stn}$[2] ‰
			initial solution		final solution		exchangeable Li		residual Mg and Li			mass fraction		bulk solid				
Reaction vessel - stevensite																		
250117	10.3	0.2416	10.4	0.9	11.2	1.4	252.6	-1.4	246.6	56.7	-11.6	0.82	0.18	183.6	309.3	-3.5	-3.9	-12.5
Bottle - stevensite - low Na series																		
010217E	10.0	0.1000	13.4	1.3	13.1	1.6	47.5	-2.3	120.7	53.5	-14.6	0.47	0.53	101.1	101.0	-8.6	-10.0	-16.0
010217F	10.3	0.1917	13.9	1.0	14.3	1.1	51.2	-2.3	107.3	33.2	-14.1	0.61	0.39	91.9	84.3	-7.8	-8.6	-15.1
Bottle - stevensite - low Mg series																		
240417B	9.5	0.0043	15.3	2.1	15.4	1.8	n.m.	n.m.	n.m.	n.m.	n.m.	n.m.	n.m.	97.2	n.m.	-12.7	n.m.	n.m.
240417J	9.7	0.0393	15.1	2.3	15.1	1.6	19.4	-7.9	87.1	46.8	-14.1	0.29	0.71	65.6	66.2	-12.7	-12.3	-16.3
240417C	9.9	0.0764	15.1	1.9	15.0	1.3	16.3	-6.9	101.9	48.7	-15.3	0.25	0.75	65.3	65.0	-13.1	-13.2	-17.1
240417D	10.2	0.0890	16.0	2.1	15.9	1.9	16.2	-5.9	113.5	39.2	-15.8	0.29	0.71	53.8	55.4	-12.6	-12.9	-17.9
Bottle - stevensite - high Mg series																		
240417E	9.0	0.0287	15.8	2.1	15.6	1.6	7.2	-9.0	67.3	21.1	-14.6	0.25	0.75	27.5	28.2	-13.0	-13.3	-16.7
240417K	9.3	0.1024	16.4	1.4	16.4	1.0	8.4	-7.1	90.2	17.3	-14.9	0.33	0.67	26.2	25.7	-12.5	-12.3	-16.3
240417F	9.5	0.1493	16.1	1.8	16.2	1.6	5.5	-4.8	109.8	17.4	-15.8	0.24	0.76	25.2	22.9	-13.4	-13.2	-17.6
240417G	9.8	0.2545	16.8	1.9	16.7	1.9	4.5	-5.3	142.6	15.5	-18.0	0.23	0.77	17.7	20.0	-14.8	-15.2	-20.0
240417H	10.0	0.3015	15.8	1.9	15.9	1.4	3.2	-7.4	147.1	6.4	-19.6	0.33	0.67	8.0	9.6	-14.8	-15.6	-21.5
240417L	10.4	0.2092	16.4	2.1	16.2	1.6	2.6	-9.5	147.7	2.4	-19.5	0.52	0.48	6.7	5.0	-15.2	-14.3	-21.6
Bottle - saponite																		
20140624F	9.5	0.2372	7.9	13.5	7.8	13.1	20.9	13.9	121.7	15.7	-3.0	0.57	0.43	32.5	36.7	6.0	6.7	-16.5

n.m. = not measured
*Calculated by mass balance
[1] 2SD 1.1‰ [2] 2SD 1.5‰

9

2.3. NMR

Room temperature solid-state magic-angle spinning (MAS) ^{7}Li-NMR (nuclear magnetic resonance) experiments for hectorite (Clay Minerals Society Source Clay SHCa-1), 20140624F and its residue were conducted on a Varian Infinity spectrometer at a magnetic field strength of 9.39 T operating at a spectrometer frequency of 155.47 MHz. The samples were packed into 4.0 mm zirconia rotors and spun at 10 kHz in a double resonance MAS NMR probe. Spectra were secondary referenced to spodumene at -1.0 ppm on a ppm scale where 0.5 M LiCl (in DI water) is 0.0 ppm, and were acquired using a single-pulse experiment with a $\pi/6$ pulse (3 μs) and a 16 s recycle delay. Similarly, ^{7}Li MAS NMR experiments for hectorite, the empty rotors, 010217F and its residue, and a rerun of 20140624F took place on a Varian Infinity-plus spectrometer operating at a spectrometer frequency of 194.21 MHz at a magnetic field strength of 11.74 T. The same 4.0 mm rotors as in the previous NMR experiment were used but with a triple resonance MAS NMR probe. Again, samples were spun at 10 kHz and spectra were acquired in a single pulse experiment with a $\pi/6$ pulse and recycle delay of 16 s. As the ceramic rotors and probe components could contain Li impurities at concentrations exceeding those of the samples studied, the empty rotors were analysed under the same conditions as the samples. Spectra acquired for the empty rotors were indistinguishable from noise and so were not subtracted from the sample spectra. Peak fitting was performed using the multi-peak fit package in Igor Pro (WaveMetrics) which uses a non-linear least squares approach to fit Gaussian and Lorentzian peaks to characteristic features observed in the NMR spectra. The percentage of Li removed from each site as a result of treatement with NH_4Cl was calculated based on the difference in number of Li atoms between the bulk and residue spectra which was calculated as follows: the areas fitted to each peak were normalised to the number of scans acquired for each sample and the mass of Li analysed in each site was calculated using a quantified spectrum of a known mass of hectorite. The mass of Li in each site was then normalised to the mass of sample analysed to obtain the concentrations of Li in each site (mg/kg) and subsequently the number of Li atoms in each site.

3. Results

3.1. Solid characterisation

Fourier Transform Infrared (FT-IR) spectroscopy and X-ray diffraction (XRD) were used to characterise the nature of the synthetic materials formed. Transmission FT-IR spectra of all products were characterised by principal Si-O stretches (~1000-1020 cm^{-1}, Fig. 2a), consistent with a 2:1 layer structure and Mg occupancy in trioctahedral sheets (Mg_3-OH stretch at 3680 cm^{-1}, Fig. 2a), as well as corresponding lattice vibration features at 544 and 464 cm^{-1} (Wilkins and Ito, 1967; Farmer, 1974; Russell and Fraser, 1994; Tosca and Masterson, 2014). The products exhibit clear *hkl* peaks at 10-15, 4.47, 3.51, 2.56 and ~1.52 Å (Fig. 2b) in powder XRD data (random mounts). These are each produced from the overlapping of multiple reflections and peak broadening produced by a relatively small coherent scattering domain and therefore small particle size (a few to one hundred nanometers). In addition, all diffraction peaks are significantly broadened relative to phases that possess long-range crystalline order, indicating
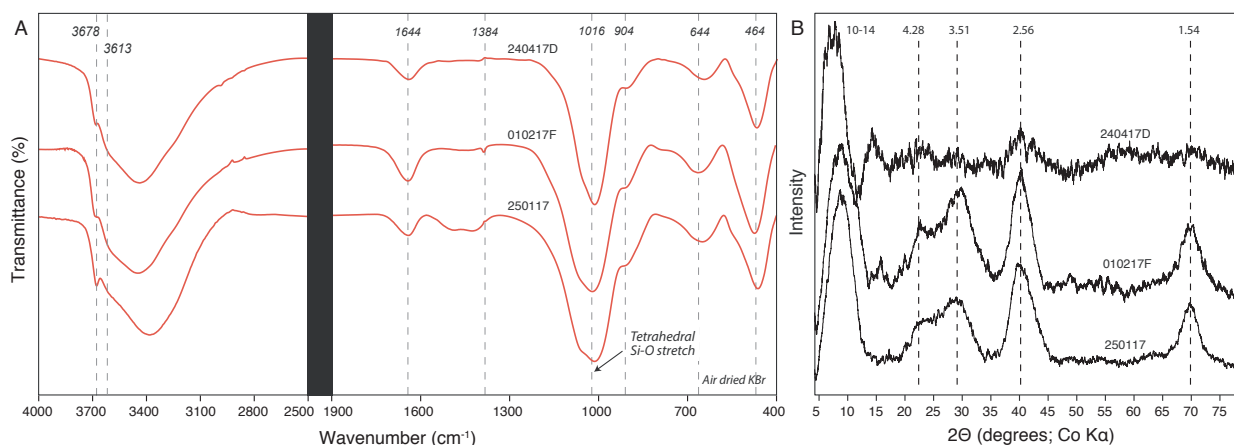
Figure 2: Three representative FT-IR (A) and powder XRD (random mounts) (B) spectra for the bulk solids formed. The key peak positions indicating the formation of a 2:1 layer trioctahedral Mg layer silicate mineral are indicated.

that, in general, the products are poorly crystalline. The peak positioned at ~1.52-1.54 Å is particularly informative because it provides independent yet complimentary evidence to FT-IR (i.e. the Mg_3-OH stretch at ~3680 cm^{-1}) that the synthetic materials have developed an ordered trioctahedral layer. Where present, the diffraction peak at ~10-15 Å provides critical information as to the nature of the precipitate. Typical powder XRD peak positions (uncorrected for polarisation effects) are commonly located at either ~10 Å or ~14 Å. As discussed in section 1.1, these peak positions are consistent with kerolite-type and stevensite-type structures, respectively. However, XRD data from oriented clay mounts suggest that this peak is largely unresponsive to ethylene glycol treatment, even after several weeks of exposure to ethylene glycol vapour at 60°C. This indicates that although the development of layer stacking order is evident along the 001 direction, ethylene glycol absorption does not take place. This may be related to strong hydration of Mg-silicate nuclei interlayers and edges (cf. TGA-DTA data in Tosca and Masterson, 2014) which may inhibit ethylene glycol absorption.

3.2. Initial, final and exchangeable solutions

Due to variable δ^7Li in the starting solutions, all data is reported as the difference between solid and initial solution δ^7Li values (Δ^7Li$_{x-solution}$). The fraction of Li from the initial solution removed into clay is ≤0.005 (Table 2) and therefore the observed variations in Li isotope fractionation are not due to variations in the fraction of Li uptake. The experiments were terminated once successive concentration measurements were within measurement error of each other, i.e. they had reached steady-state with respect to concentration measurements (Figure S1).

The concentration of exchangeable Li varied from 3 to 51 mg kg^{-1} (excluding the reaction vessel experiment, section 3.5). Exchangeable δ^7Li values were higher than the corresponding bulk δ^7Li value but were lower than the starting solution δ^7Li value by an average of 7‰ (Fig. 3, Table 2).
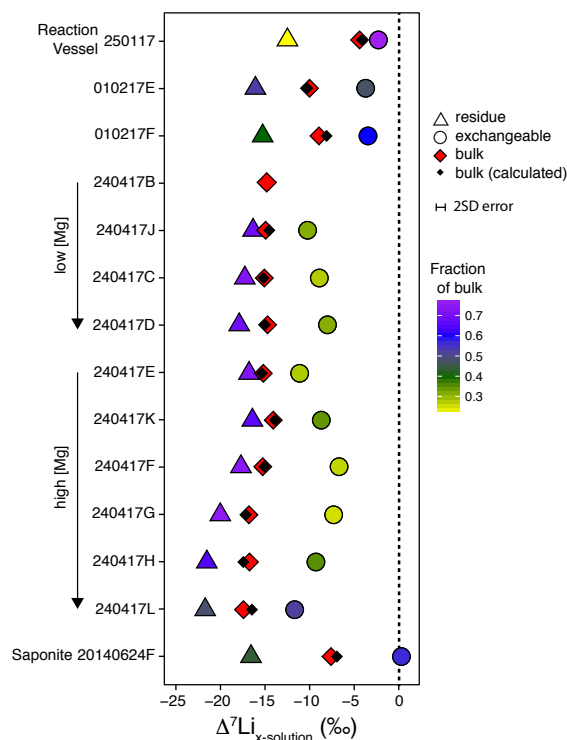
11

Figure 3: Summary of the Li isotopic compositions for the exchangeable, residual and bulk phases for each of the experiments. The calculated δ^7Li derived from mass balance is shown for comparison. The colour gradient of the exchangeable and structural (residue) Li pools reflects the fractional contribution of those pools to the bulk. All Li isotopic compositions are plotted relative to the initial solution which is at 0‰ in this plot and highlighted by the dotted line. The arrows for the high and low [Mg] series of experiments indicate increasing pH towards the head of the arrow.

3.3. NMR to assess the efficiency of the cation exchange procedure

The efficiency of the removal of exchangeable ions by NH$_4$Cl was checked using ^{7}Li-NMR. Due to the differing bonding environments, the induced magnetic field experienced by structural (octahedral) Li is expected to be different compared to exchangeable Li and therefore have a different chemical shift. We observe three peaks in the ^{7}Li-NMR spectra (Fig. 4) of the solid recovered from both a saponite (20140624F) and a stevensite (010217F) experiment demonstrating that three bonding environments are present. Based on a comparison with the spectra of the hectorite standard SHCa-1, which only contains octahedral Li, we conclude that the largest peak (peak 3), with the most negative shift, is the octahedral site (Fig. 4). This peak is also least affected by the exchange procedure (Fig. 4, Table 3), consistent with Li incorporated into the clay structure. The assignment of the remaining two peaks is discussed in section 4.1.

The peak area is proportional to the number of Li atoms in each bonding environment and the results of the peak fitting are used to calculate the relative proportion of Li in each (Table 3). For the 20140624F sample, addition of NH$_4$Cl resulted in 81±6%, 58±16% and 3±5% loss of Li from peaks 1, 2 and 3 respectively and for the 010217F sample the equivalent values were 66±3%, 62±9% and 18±2% (Table 3). The significant loss of Li from peaks 1
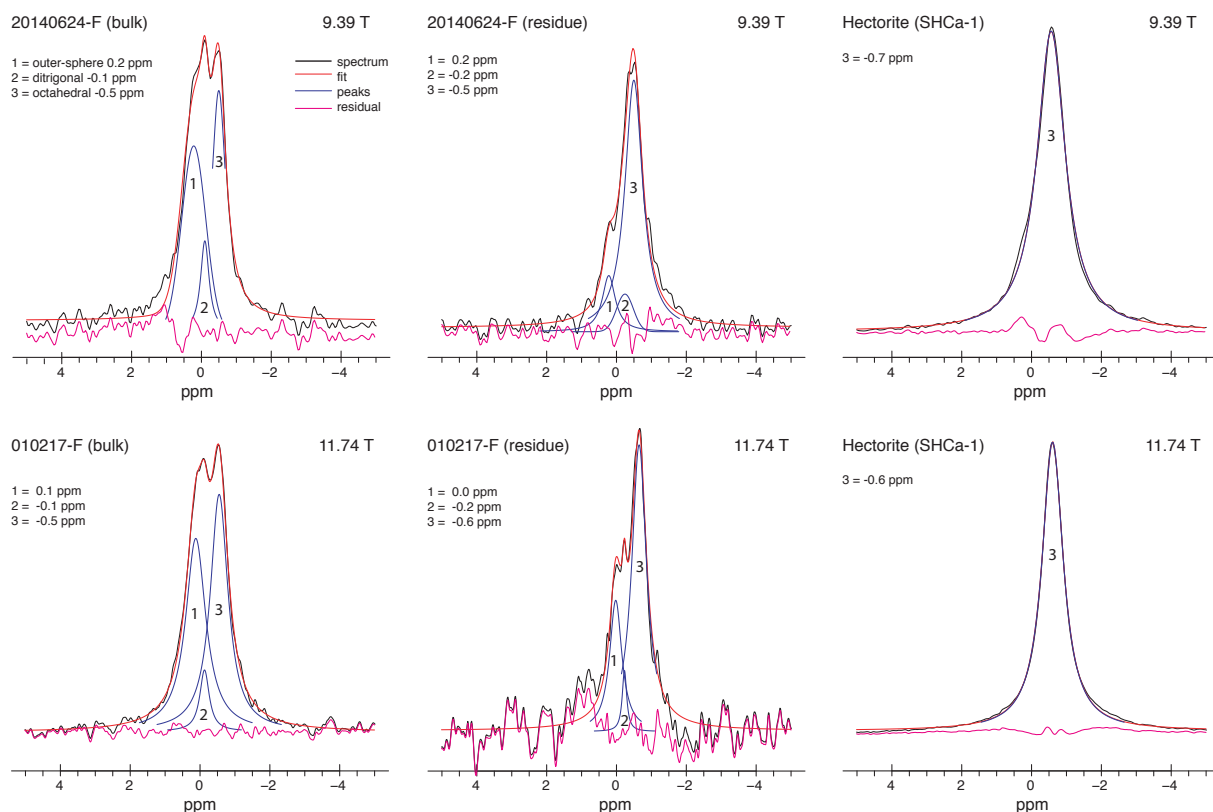
Figure 4: NMR spectra. Top row spectra were collected at 9.39 T (400 MHz) whereas bottom row spectra were collected at 11.74 T (500 MHz). Note the decrease in both the outer-sphere and pseudo-hexagonal peaks (peaks 1 and 2) in the residual (after treatment with NH$_4$Cl) sample spectra compared to the bulk sample spectra. The resolution (FWHM - full width at half maximum) in peak position is ± 0.1 ppm.

and 2 supports the contention that these sites represent exchangeable Li. Although a significant proportion of Li from peaks 1 and 2 is removed as a result of the exchange procedure, 13-26% peak 1 Li and 4-7% peak 2 Li remains in the residual solid (Table 3). Assuming these samples are representative, the exchange procedure, although effective, has not removed all of the exchangeable Li and some remains in the residual solid. Equally, some octahedral Li was lost during the exchange procedure. The total fraction of exchangeable Li calculated from NMR (40±7% 20140624F, 43±3% 010217F) is in agreement with that calculated from concentration measurements (57±4% 20140624F, 61±3% 010217F (f$_e$ in Table 2), Table 3).

3.4. Bulk and residual solids

All solids were enriched in ^{6}Li compared to the starting solution (Fig. 3, Table 2). The bulk solids had δ^7Li values 4.4 to 17.3‰ lower than the initial solution and the δ^7Li values of the residual solids were lower than the corresponding bulk δ^7Li value by 1.4 to 9.0‰ (Fig. 3, Table 2). The bulk solids contained 7 to 184 mg kg^{-1} Li whilst the concentration of Li in the residual phase varied from 2 to 57 mg kg^{-1} (Table 2).

There is no relationship between pH and Δ^7Li$_{bulk-solution}$ values (Fig. 5a), even when pH was varied systematically ('240417' series). However, covariation between pH and Δ^7Li$_{residue-solution}$ values (exchangeable Li removed) is
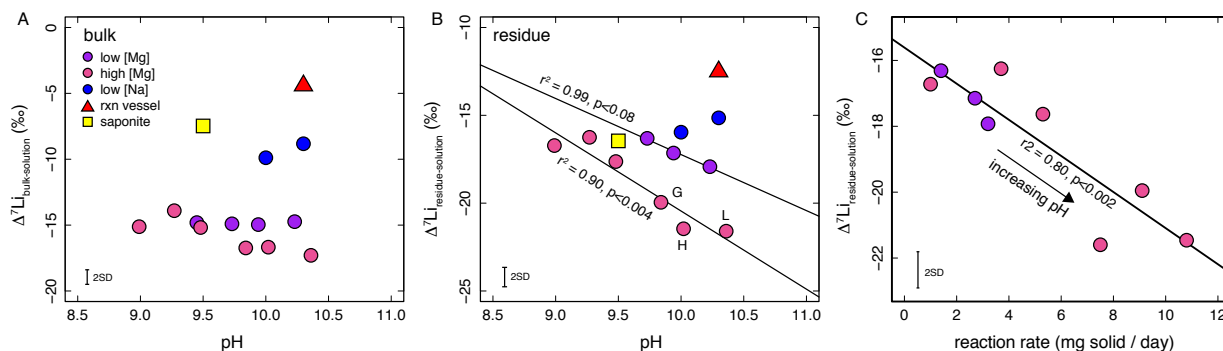
13

Figure 5: Dependence of δ^7Li values on pH in the bulk (A) and residual (B) solids. In the high [Mg] series of experiments there is a trend of decreasing Δ^7Li$_{residue-solution}$ values with increasing pH. (C) Higher reaction rates (mass of solid produced per day) are associated with lower Δ^7Li$_{residue-solution}$ values.

observed in the '240417' series of experiments (Fig. 5b). Whilst reaction rate could be one factor affecting the Δ^7Li$_{residue-solution}$ values (Fig. 5c), another factor could be the solution chemistry. The stevensite experiments were conducted at constant Li concentration in the initial solution but with varying Na, Mg, and H$^+$ concentrations (Table 1). For similar pH (10.0 - 10.4), higher [Na] concentrations in the initial solution were associated with a greater difference in δ^7Li values between the bulk solid and the initial solution (Fig. 6a). For pairs of experiments conducted at similar pH, higher [Mg] is linked to lower Δ^7Li$_{residue-solution}$ and lower Li/Mg values in both bulk and residual solids (Table 2). The Li/Mg ratios of the residual solids ranged between 1.6×10^{-5} and 5.3×10^{-4} mg kg^{-1}/mg kg^{-1} and there is a relationship between the Li/Mg ratios of the residual solids and Δ^7Li$_{residue-solution}$ values in experiments with constant Mg concentration (Fig. 7).

3.5. Mass balance

The exchangeable and residual Li concentrations (calculated relative to the bulk sample) were summed and compared to the measured bulk concentrations. Calculated bulk Li concentrations are within 15% of measured bulk Li values except for 240417H (18%), 240417L (25%) and the reaction vessel experiment (72%). The poor agreement between calculated and measured bulk values for the reaction vessel experiment implies the results from this experiment should be treated cautiously. The percentage of Li in the exchangeable and residual pools was calculated relative to the calculated bulk value and these were used to calculate the isotopic composition of the bulk which agreed with the measured value to within 1.5‰ (Fig. 3), demonstrating the self-consistency of the methodology.

4. Discussion

Our experiments confirm the results of previous laboratory experiments (Vigier et al., 2008) which found that hectorite preferentially incorporates ^{6}Li and are also in agreement with the direction of Li isotope fractionation inferred from field studies (e.g. Huh et al., 2001) and modelling studies (Dupuis et al., 2017). There is considerable variation
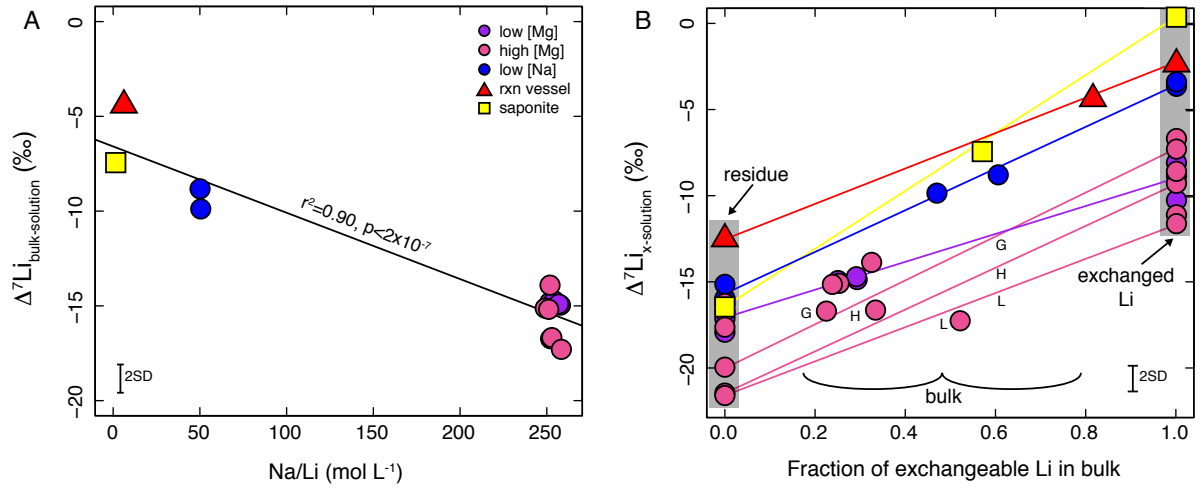
14

Figure 6: (A) Plot of $\Delta^7\text{Li}_{bulk-solution}$ vs Na/Li in the initial solution. The more Na, the lower the $\Delta^7\text{Li}_{bulk-solution}$ value consistent with less outer-sphere Li. (B) Plot of $\Delta^7\text{Li}$ versus the fraction of exchangeable Li. The greater the fraction of exchangeable Li, the higher the $\Delta^7\text{Li}_{bulk-solution}$ value consistent with less competition from Na. $\Delta^7\text{Li}_{bulk-solution}$ values are a mixture between residual Li (octahedral≫outer-sphere>pseudo-hexagonal) and exchangeable Li (outer-sphere≫pseudo-hexagonal≈octahedral). The $\Delta^7\text{Li}_{bulk-solution}$ values are within error of the lines connecting these two end-members. For the low [Na] (blue circles) and the [Mg] experiments (pink/purple circles, excluding G, H and L), the average for each end-member (residual and exchangeable) is used. Variations in the positions and slopes of the lines are likely due to varying proportions of the three Li sites (octahedral, pseudo-hexagonal and outer-sphere) in each of the end-members. For example, 20140624F (yellow square) contains more outer-sphere Li ($\delta^7\text{Li}$~0‰, Section 4.1) than 010217F (blue circle) in the exchangeable fraction but less outer-sphere Li in the residue (Table 3) resulting in a mixing line with a steeper slope.
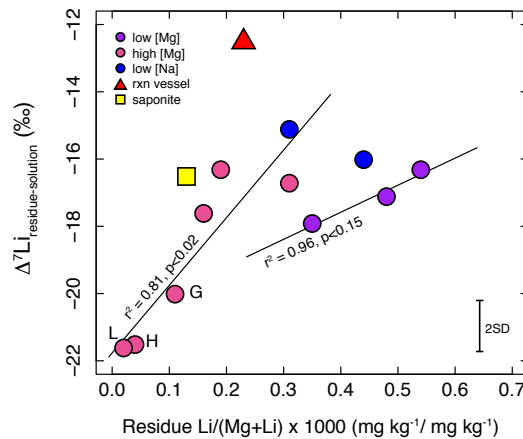

Figure 7: Dependence of $\delta^7\text{Li}$ values in the residual phase on solid composition. In sets of experiments where only pH varies (pink and purple points), $\Delta^7\text{Li}_{residue-solution}$ values increase with increasing Li/(Mg+Li).

Table 3: Results from ^{7}Li-NMR peak fitting. Peak numbers refer to Fig. 4.

Experiment	Sample	Octahedral Peak 3 %	Pseudo-hexagonal Peak 2 %	Outer-sphere Peak 1 %	Li removed		$\Delta^7Li_{bulk-solution}$ ‰
					NMR (%)	Conc[1] (%)	
20140624F	Bulk	49±1	11±1	40±1			-7.5
	Residue	80±1	7±1	13±1			-16.5
	Exchangeable[2]	4±6	15±5	81±15			0.4
	Removed[3]	3±5	58±16	81±6	40±7	57±4	
010217F	Bulk	48±0	7±0	45±0			-8.8
	Residue	69±1	4±1	26±1			-15.1
	Exchangeable[2]	21±3	10±2	70±5			-3.3
	Removed[3]	18±2	62±9	66±3	43±3	61±4	

[1]Calculated by mass balance based on measured Li concentrations (Table 2).
[2]Calculated based on loss of Li from bulk.
[3]Percentage of Li removed from a given bulk spectra peak as a result of the exchange procedure.

in the residual and bulk Δ^7Li values (Fig. 3) and in the following sections we will discuss some experimental factors, including the bonding environment and chemistry of the initial solution (including pH), which could cause this variation.

4.1. Li fractionation associated with different bonding environments

In a layer silicate structure Li is located in octahedral sites. Due to its small size Li can also be located in pseudo-hexagonal sites (ditrigonal cavity) in the tetrahedral sheet, interlayer sites between TOT layers and be adsorbed onto surfaces (Fig. 1, Meunier, 2005). The combination of isotopic analyses of exchangeable solutions, bulk and residual solids, coupled to ^{7}Li-NMR provides a unique way to deconvolve the relative Li isotope fractionation between distinct bonding environments. Three peaks are observed in the ^{7}Li-NMR spectra and two of these decrease markedly in area after saturation with NH$_4$ (peaks 1 and 2, Fig. 4), confirming that the exchange procedure was effective at removing exchangeable Li but that some remained in the residual solid (Table 3). If the uptake of Li into a non-octahedral site has a unique fractionation factor then the presence of Li in these sites in the residual phase would mean that the δ^7Li value of the residual phase can no longer be assumed to represent fractionation into octahedral sites only. Below we discuss what is known about the bonding environments of Li to assign each ^{7}Li-NMR peak to a specific bonding environment and assess the magnitude of Li isotope fractionation in the three environments relative to each other.

Peaks 1 and 2 in the ^{7}Li-NMR spectra correspond to exchangeable Li. These were assigned based on coordination number as chemical shift is dependent on coordination number, with a lower coordination number resulting in less shielding and a more positive chemical shift (Xu and Stebbins, 1995). Chemical shift ranges for Li with coordination numbers 4 and 6 taken from ^{6}Li-NMR spectra (same chemical shift as ^{7}Li-NMR) are 0 to 1 ppm and -0.3 to -1.3 ppm, respectively (Xu and Stebbins, 1995). For smectites, both interlayer and adsorbed Li are thought to exist as outer-sphere complexes with a coordination number of 4 (hydrated Li, Pistiner and Henderson, 2003; Chan and Hein, 2007) and are therefore expected to experience the same chemical shift. In the following discussion these two sites are therefore grouped together as 'outer-sphere' sites. In contrast, pseudo-hexagonal Li exists in an inner-sphere complex with O^{2-} atoms and, due to distortions, has an effective coordination number of 6 (Meunier, 2005). Allowing for the
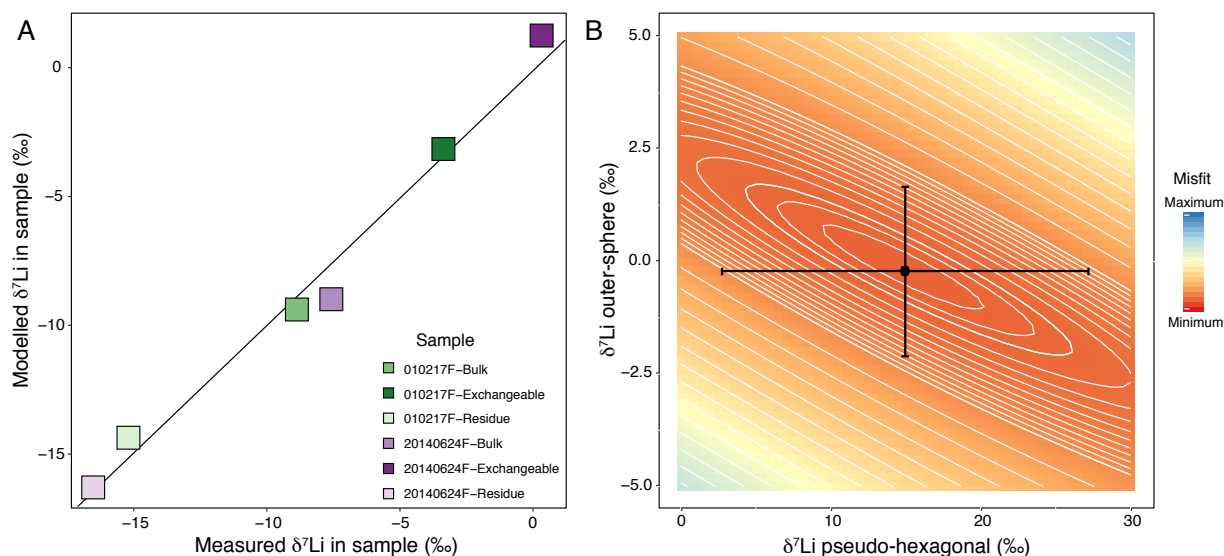
Figure 8: (a) Comparison of the measured δ^7Li values (Table 2) with the modelled δ^7Li values of the samples, calculated using the fractionation factors obtained through a Monte Carlo minimum misfit method and the proportions of Li in each bonding environment calculated from ^{7}Li-NMR (Table 3). The black line is the 1:1 line. (b) Example of a misfit contour plot in 2-D space (octahedral δ^7Li value set at the minimum misfit value of -21.5‰ in order to make a 2-D plot). The calculation of the misfit is described in the supplementary information. The black point indicates the optimum (smallest misfit) values for outer-sphere and pseudo-hexagonal bonding environments. 1σ error bars are also shown.

317 fact that ^{7}Li-NMR peaks are broader than ^{6}Li-NMR peaks, the chemical shift of the most positive peak (peak 1: 0.0 to

318 0.2 ppm) is in agreement with 4-fold coordinated outer-sphere Li and the negative chemical shift of the middle peak

319 (peak 2: -0.1 to -0.2), 6-fold coordinated pseudo-hexagonal Li. The assignment of peak 2 to pseudo-hexagonal Li

320 is consistent with this site having a more similar bonding environment (same coordination number) to octahedral Li

321 compared to outer-sphere Li and therefore its chemical shift is closer to the octahedral peak (peak 3). The contrasting

322 δ^7Li values between exchange solutions and residual solids implies that each bonding environment has its own isotope

323 fractionation factor. Our data cannot directly constrain the three fractionation factors but a system of linear equations

324 can be solved based on the parameters in Table 3 (6 equations, 3 unknowns). A Monte Carlo minimum misfit method

325 (Supplementary Information) was employed. The fractionation factors for the three bonding environments determined

326 using this method were: octahedral -21.5±1.1‰, outer-sphere -0.2±1.9‰ and pseudo-hexagonal 15.0±12.3‰ (errors

327 1σ, Fig. 8).

328   Previous studies have suggested that both interlayer Li and Li adsorbed to smectites have the same isotopic com-

329 position as the starting solution since Li in both cases is held in weakly bonded outer-sphere complexes (Pistiner

330 and Henderson, 2003; Chan and Hein, 2007). Interlayer Li should in theory retain its 4-fold coordinated hydration

331 sphere (and therefore not be fractionated), however it has been suggested that in addition to outer-sphere complexes,

332 inner-sphere (dehydrated) complexes may also form in the interlayer where the solvation number can vary from 2 to

333 4 (Greathouse and Sposito, 1998). If the coordination number of Li in the interlayer does decrease below 4, then this

334 Li will be enriched in ^{7}Li relative to the initial solution (Wimpenny et al., 2015). Our fitting results suggest that the

17

fractionation factor for outer-sphere complexes is within error of zero, supporting the former hypothesis; that interlayer Li is unfractionated with respect to the starting solution (Pistiner and Henderson, 2003; Vigier et al., 2008), and therefore likely remains in a 4-fold coordination.

Whilst outer-sphere Li is not fractionated significantly relative to the starting solution, octahedral Li is, with a value of -21.5±1.1‰. This finding is consistent with isotope equilibrium theory where strong bonds with a high vibrational frequency will always favour the heavy isotope because the vibrational frequency of the bond scales with the square root of the bond strength over reduced mass (Bigeleisen, 1965). Typically, bond strength scales with bond length, such that shorter bonds are stronger. Li in octahedral sites is bonded to oxygen atoms in a six-fold coordination with a bond length of around 2.08 Å (sodium fluorohectorite, Kalo et al., 2012) whereas Li in the aqueous phase exists predominantly as the $[Li(H_2O)_4]^+$ species with a bond length of around 1.9 Å (Rudolph et al., 1995; Mähler and Persson, 2012). Therefore octahedral Li, with a longer, weaker bond will be enriched in ^6Li compared to the initial solution as calculated, and predicted by both density functional theory (DFT) calculations (Dupuis et al., 2017) and experimental data (Fig. 3, Vigier et al., 2008).

Pseudo-hexagonal Li has been assumed to have the same fractionation factor as the octahedral site (Williams and Hervig, 2005) based on both sites having a coordination number of 6 (Meunier, 2005). Nevertheless, the bonding environment of the pseudo-hexagonal and octahedral sites is different as evinced by the different chemical shifts in ^7Li-NMR spectra (Fig. 4, Theng et al., 1997) and could therefore be expected to have different fractionation factors. The looser bound pseudo-hexagonal Li may have longer Li–O bonds compared to the octahedral sites, and this is supported by a DFT calculation demonstrating that the Li sits asymmetrically in the pseudo-hexagonal site with Li–O bond lengths varying from 2.01 to 3.91 Å (Wungu et al., 2011). This would result in a longer average bond length compared to octahedral Li and we would therefore predict a lower δ^7Li value. However, the results from the Monte Carlo calculation suggest that pseudo-hexagonal Li is enriched in ^7Li compared to the initial solution (Fig. 8a), which is inconsistent with the ^7Li-NMR peak position. The bonding environment with lowest coordination number (outer-sphere Li) should have the highest chemical shift (Xu and Stebbins, 1995) and therefore the highest δ^7Li value. However, we note that the calculated isotope fractionation for the pseudo-hexagonal site is subject to large uncertainty which strongly co-varies with the δ^7Li value of outer-sphere Li (Fig. 8b). If the pseudo-hexagonal value was reduced to 0‰, this would shift the outer-sphere δ^7Li value by <2.5‰ (Fig. 8b). As more synthetic clay samples are measured by ^7Li-NMR and for δ^7Li, the uncertainty in the pseudo-hexagaonal δ^7Li value will reduce.

In summary, there are unique Li isotope fractionation factors for the three bonding environments observed in ^7Li-NMR spectra (octahedral, outer-sphere and pseudo-hexagonal) and bulk, exchangeable and residual phases contain variable proportions of all three, leading to the observed variability in δ^7Li values in these phases (Fig. 3). Therefore it is essential that the potential for remaining interlayer, adsorbed and pseudo-hexagonal Li is taken into account when using the residual phase to infer a fractionation factor for Li uptake into octahedral sites.

4.2. pH dependence

The main experimental variable which changed between the different experiments was pH. Increasing pH increases nucleation rate, growth rate and promotes better crystallisation and therefore reaction rates scale with pH (Table 2). There is no correlation between pH and $\Delta^7Li_{bulk-solution}$ and this is most likely due to the variable contribution of exchangeable Li, with a distinct fractionation factor, to the bulk Li isotopic composition (Fig. 5a). However, there is a strong relationship between pH and $\Delta^7Li_{residue-solution}$ (Fig. 5b). It is possible that the trend of more negative $\Delta^7Li_{residue-solution}$ values with increasing pH observed in the '240417' series of experiments (low and high [Mg], Fig. 5b) is the result of a kinetic isotope fractionation effect. Indeed, for these experiments, the $\Delta^7Li_{residue-solution}$ values decreased as reaction rate (mg solid formed per day) increased (Fig. 5c), consistent with increased kinetic fractionation at higher pH as observed for Ca isotope fractionation during calcite synthesis (Tang et al., 2008; Nielsen et al., 2012).

However, pH can also affect the Li speciation in solution (Bogatko et al., 2013) and a recent study attributed a relationship between δ^7Li and pH in foraminifera to changes in Li speciation (Roberts et al., 2018). The aqueous speciation of Li is not well defined but Li can be considered to be a very weak acidic cation with aqua (e.g. $Li(H_2O)_x^+$) and hydroxo forms (e.g. $Li(OH)(H_2O)_{x-1}$), most likely with a secondary hydration shell (Bogatko et al., 2013). These two forms have different desolvation energies and as the isotope exchange equilibrium constant is greater than 1, the isotopic composition of a solid precipitating from solution will depend on the relative proportion of these two forms in solution. Bogatko et al. (2013) calculated that for the precipitation of carbonate from solution at 25°C the $\Delta^7Li_{CO_3^{2-}-H_2O}$ value decreased when, depending in the exact model parameters used, pH increased above ~9. Therefore the lower $\Delta^7Li_{residue-solution}$ values we observe in this study when increasing pH from 9.0 to 10.4 (Fig. 5b) would be consistent with a change in aqueous Li speciation. As pH increases the Mg/Li ratio of the residual solid also increases which may additionally impact on the $\Delta^7Li_{residue-solution}$ value (Section 4.3). Further experimental work would be required to assess whether equilibrium or kinetic fractionation is dominant.

4.3. Composition dependence

The initial solution composition will likely affect the crystallisation process and our experiments were conducted at a range of Si, Na, Mg and Al concentrations (Table 1). For the bulk solids, lower Na concentrations in the initial solutions are associated with smaller $\Delta^7Li_{bulk-solution}$ values (Fig. 6a) and the lower the Na concentration, the greater the fraction of exchangeable Li in the bulk solid (Fig. 6b). These observations may be a result of competition between Na and Li for interlayer sites (Tutolo and Tosca, 2018). If it is assumed that interlayer Li has an isotopic composition similar to the initial solution, an increased fraction of interlayer Li in the bulk solid would increase the bulk Li isotopic composition. On the other hand, in the experiments with high Na concentrations, Na outcompetes Li, reducing the fraction of interlayer Li in the bulk solid. After treatment to remove exchangeable cations, we do not find significant differences in $\Delta^7Li_{residue-solution}$ values between experiments with different initial Na concentrations (Fig. 6b), if the reaction vessel and three high pH, high [Mg] experiments are excluded due to additional factors related to pH (Section

4.2). The lack of control of initial solution compositions on the residual solid Li isotopic composition is in agreement with previous studies (Vigier et al., 2008; Wunder et al., 2006).

The composition of the solid itself appears to have a negligible effect on $\Delta^7\text{Li}_{residue-solution}$ values: the synthetic saponite has a similar value to the low [Mg] stevensite experiments (Fig. 3). This is in agreement with a modelling study which predicted only a minor difference ($\leq 1.0‰$) between a Li-Mg and a Li-Al phyllosilicate (Dupuis et al., 2017). However, there is a hint in the data that the balance between Mg and Li in the residual solids could affect the $\Delta^7\text{Li}_{residue-solution}$ value, with lower Li/Mg ratios associated with lower $\Delta^7\text{Li}_{residue-solution}$ values (Fig. 7). Even at equilibrium, a change in element ratio is predicted to affect isotope fractionation due to changes in bond lengths as the crystal structure distorts to accommodate an ion with a different charge and/or radius (Perdikatsis and Burzlaff, 1981; Brigatti et al., 2000; Laurora et al., 2011; Michalski et al., 2015; Wang et al., 2017a,b). A decrease in the Li content of the residual solid could therefore cause the Li–O bond length to change, impacting the fractionation factor for the octahedral site. It is also important to consider exactly how the Li ends up in an octahedral site. A study on Mg-Fe substitution in dioctahedral clay minerals found that entering into a vacant octahedral site or substituting into an already filled octahedral site had opposite effects on bond length (Michalski et al., 2015). Further modelling and experimental data would be required to see if changes in bond length could explain the relationship between Li/Mg and $\Delta^7\text{Li}_{residue-solution}$ values (Fig. 7).

However, bond length arguments assume equilibrium isotope fractionation is occurring and it also assumes that all Li in the residue is in octahedral sites. As we discussed in section 4.1, variable proportions of exchangeable Li remaining in the residual solid could impact on the Li isotopic composition of the residue. Based on the fact that the $\Delta^7\text{Li}_{residue-solution}$ values of H and L (-21.5 and -21.6‰) are within error of the fractionation calculated for the octahedral site (-21.5‰), these samples may contain a negligible proportion of exchangeable Li. The higher reaction rate of these experiments (Fig. 5c) could have resulted in larger particles decreasing the proportion of exchangeable Li held on surface and edge sites. The high pH of experiments G, H and L may also change the speciation of Li in solution (section 4.2) which could contribute to the trend observed in Fig. 7.

4.4. Temperature dependence

In equilibrium isotope fractionation there is often a linear relationship between the fractionation factor and the reciprocal of temperature squared, with greater fractionation at lower temperatures (Schauble, 2004). Vigier et al. (2008) argued that the good reproducibility of several experiments conducted at a single temperature under different conditions indicated the lack of kinetic isotope effects and that the synthesised clays had reached isotopic equilibrium. Our experiments reach chemical equilibrium (Figure S1) and the majority of the isotope data also reproduce very well (Fig. 9). The overall average $\Delta^7\text{Li}_{residue-solution}$ is -17.3±5.0‰ (2SD), where this value represents a mixture of octahedral and exchangeable Li. The lower $\Delta^7\text{Li}_{residue-solution}$ values of samples G, H and L and the higher value for the reaction vessel experiment compared to the other samples could relate to kinetic or equilibrium controls as discussed in sections 4.2 and 4.3. If these values are excluded, the average $\Delta^7\text{Li}_{residue-solution}$ is -16.6±1.7‰ (2SD).
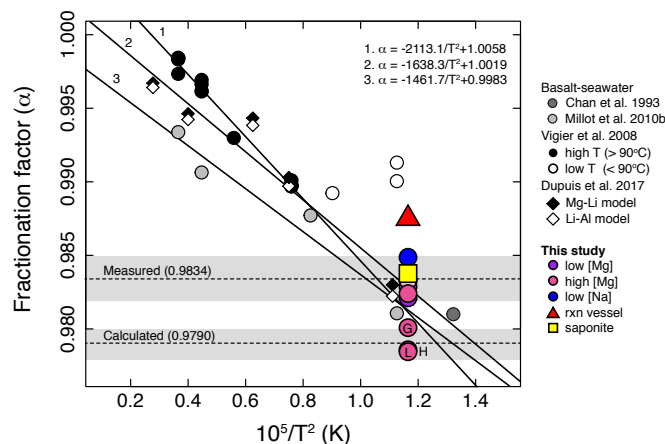
20

Figure 9: Fractionation factor dependence on temperature. Equilibrium fractionation factors are calculated from the Li isotopic compositions of the initial solution and residual solid using the relationship $\alpha = (1000-\delta^7Li_r)/(1000-\delta^7Li_i)$. Literature data were compiled from synthesis experiments (Vigier et al., 2008), modelling (Dupuis et al., 2017) and basalt-seawater interaction experiments (Millot et al., 2010b; Chan et al., 1993). In the latter, solids were not treated to remove exchangeable Li. We do not include experiments conducted at high pressure (Wunder et al., 2006, 2007, 2010). Regression lines for each set of literature data are plotted. Line 1 only includes high temperature experiments (see Vigier et al. (2008) for details) and the line for basalt-seawater (line 3) only includes data from Millot et al. (2010b). Note that in the Millot et al. (2010b) study, the solids were not measured directly and were shown to contain a mixture of phases including Li from seawater and the original basalt. The dotted line marked 'measured' indicates the average α at 20°C for the measured residual fractions (assuming complete removal of exchangeable Li), excluding the reaction vessel and G, H and L (see text for details). The dotted line marked 'calculated' indicates the octahedral fractionation factor calculated using mass balance and ^{7}Li-NMR data (Section 4.1, Supplementary Information). The grey shaded areas indicate the 2SD error for the 'measured' line and the 1σ error for the 'calculated' line.

As the fraction of Li lost from solution is ≤0.005, we assume that $\Delta^7Li_{residue-solution}$ is equivalent to α with a value of 0.9834±0.0017. This value is in good agreement with fractionation factors predicted for 20°C based on linear regression of previously published experimental data (0.9812 (Vigier et al., 2008) and 0.9813 (Millot et al., 2010b)). Nevertheless, we know from ^{7}Li-NMR data that the residual phase contains some exchangeable Li and therefore the 'true' fractionation factor into the octahedral site will be lower than 0.9834, and is calculated to be 0.9790±0.0011 (Section 4.1). For comparison, a value of 0.9828 at 20°C was obtained from a linear regression of results from a TI-PIMD (thermodynamic integration path-integral based molecular dynamics) (Fig. 9, Dupuis et al., 2017).

Vigier et al. (2008) also conducted low temperature experiments but these had δ^7Li values approximately 7‰ higher than those predicted based on a regression line defined by the high temperature samples. It was postulated that this may have been due to low crystallinity and a high proportion of edge octahedra in the solids formed at low temperature, resulting in additional kinetic fractionation effects. Similar processes may also be impacting our reaction vessel experiment (red triangle, Fig. 9) where the actual nucleation rate may have been higher as a consequence of increasing the pH of a weakly acidic solution of Mg and SiO_2, potentially producing smaller particles with more defects and a greater proportion of edge octahedra sites. Alternatively, a consequence of the low crystallinity may be that a greater proportion of exchangeable Li remained in the residual solid after exchange with the preferred NH_4 cation.

21

4.5. Implications for field and modelling studies

The $\Delta^7Li_{solid-solution}$ value is a critical parameter for modelling weathering processes, in particular the relative balance between dissolution and precipitation reactions (e.g. Bouchez et al., 2013; Dellinger et al., 2015; Pogge von Strandmann and Henderson, 2015). Importantly, as we show in this study, the $\Delta^7Li_{bulk-solution}$ value is comprised of three separate fractionation factors corresponding to the three bonding environments visible in ^7Li-NMR spectra: octahedral, pseudo-hexagonal and outer-sphere. The value of $\Delta^7Li_{solid-solution}$ in natural systems is thus influenced by the relative proportions of Li in each of these three environments and the consequent variation in $\Delta^7Li_{solid-solution}$ could have implications for the global Li budget of seawater as illustrated below in a very simplistic manner.

The current best estimate of the δ^7Li input to the world's oceans is a flux weighted mean from large rivers with a value of +23‰ (Huh et al., 1998), which has been widely adopted in modelling studies (e.g. Li and West, 2014). At a global scale, the average continental rock drained is approximately -0.9‰ (Fig. 10), in agreement with the average δ^7Li in the upper continental crust (0±2‰, Teng et al., 2004), and hence $\Delta^7Li_{solid-solution}$ has an average value of -23.9±3.1‰ (1σ error). This value is not a fractionation factor, but is a global difference between large river and rock/sediment δ^7Li values. Interestingly, this value is within uncertainty of the octahedral fractionation factor calculated in the present study (-21.5±1.1‰). Thus it could be argued that Li incorporation into the octahedral site dominates fractionation at a global scale and that, to a first order, rivers are in equilibrium with their sedimentary products. However, we note that it is unlikely that natural clays will only contain octahedral Li. Exchangeable Li will very likely be present and may be derived from a different fluid than octahedral Li, due to changes in solution composition during mineral growth (Williams and Hervig, 2005). Therefore an assessment of equilibrium fractionation in field data would first require the removal of exchangeable Li.

A further observation is that the difference between seawater (+30.8‰, Rosner et al., 2007) and the riverine input to the oceans based on large rivers (+23‰) is 7.8‰. The difference between this value and the $\Delta^7Li_{solid-solution}$ value (-24‰) has been interpreted as a balance between high temperature formation of clays with a low fractionation factor and low temperature clays with a high fractionation factor (Li and West, 2014). Recognising that bulk solids likely contain a fraction of exchangeable Li, another potential explanation could be that, compared to the continental environment, the proportion of Li in exchangeable sites is greater in the marine environment, reducing $\Delta^7Li_{solid-solution}$. However, this would be inconsistent with our results which suggest that the higher Na concentrations in seawater would lead to a reduced fraction of exchangeable Li in bulk solids (Fig. 6).

When the δ^7Li of small rivers are considered in addition to the large rivers (compiled as a histogram in Fig. 10), the riverine input value is +16.5‰ (defined by the mode of the density function, Fig. 10), significantly lower than the flux weighted estimate from large rivers (+23‰, Huh et al., 1998). The difference between seawater and the river input would then be 14.3‰ and if this difference was only caused by the precipitation of marine clays then this apparent fractionation factor would be similar to the difference between rivers and sediments (17.3‰, Fig. 10). These values are similar to the average $\Delta^7Li_{residue-solution}$ value (-16.6±1.7‰, Fig. 9). If the δ^7Li value for the riverine input to seawater is closer to the modal value of smaller rivers rather than large rivers then it could imply a greater role of low

22

temperature reverse weathering processes on the sea-floor as being an important sink for Li (cf. Li and West, 2014). Alternatively it could imply that regardless of the type of clay or initial solution conditions (marine vs continental), the clays formed contain roughly a similar proportion of Li in the different bonding environments, supporting previous suggestions that $\Delta^7Li_{solid-solution}$ is neither affected by the initial solution composition (Vigier et al., 2008) nor the type of clay mineral forming (Dupuis et al., 2017; Pogge von Strandmann et al., 2017a).

These conflicting possibilities highlight the importance of understanding isotope fractionation processes at an atomistic scale in order to decipher global processes, and reinforces the need for further experimental isotopic and material characterisation of mineral phases. The potential implications discussed above should be treated with caution not only because of the large uncertainty, particularly on the pseudo-hexagonal fractionation factor, but also because of our limited understanding of field data and kinetics. For example, a fractionation factor ($\Delta^7Li_{solid-solution}$) of -30‰ for the uptake of Li into secondary minerals during weathering was calculated by Bouchez et al. (2013) from a steady-state mass-balance weathering model and the authors suggested that this could indicate kinetic processes superimposed on equilibrium fractionation. In summary, additional experimental work is essential to provide a better quantitative constraint on field data.

5. Conclusions

We have synthesised Mg-rich layer silicate minerals at temperatures relevant for Earth surface processes, characterising the mineralogy, structure, bonding environment and Li isotope composition. ^{7}Li-NMR data reveals that the composition of bulk clays is a mixture Li located in three bonding environments: octahedral, outer-sphere complexes (interlayer and adsorbed) and pseudo-hexagonal. Following cation exchange with ammonium chloride to remove exchangeable Li (outer-sphere and pseudo-hexagonal), the measured $\Delta^7Li_{residue-solution}$ value was -16.6±1.7‰ at 20°C, which agrees well with the apparent fractionation factor obtained from a global compilation of field data (-17.1‰) and is in agreement with previous experimental estimates for this temperature (-18.8‰, Vigier et al., 2008). However, ^{7}Li-NMR data shows that, although significantly reduced, some exchangeable Li remains in the residual solid. Once the proportions of Li in the three bonding environments are accounted for, our calculated estimate of the fractionation factor into octahedral sites is -21.5±1.1‰, slightly lower than a previous modelled value based on a density functional theory (DFT) calculation (-17.2‰, Dupuis et al., 2017). Our calculated fractionation factors for Li incorporation into outer-sphere (interlayer and adsorbed) and pseudo-hexagonal sites are -0.2±1.9‰ and 15.0±12.3‰ respectively. However, caution should be exercised when applying these values to natural clay samples as exchangeable and octahedral Li may be derived from different fluids if the isotopic composition of the fluid has evolved over time.

Our data also suggest that controls on the magnitude of the $\Delta^7Li_{residue-solution}$ value, which are also relevant to natural clays in field settings, relate to both pH, perhaps via a change in aqueous speciation or a kinetic rate control, and to the composition of the final solid (in particular the Mg/Li ratio). Combining experimental approaches with detailed
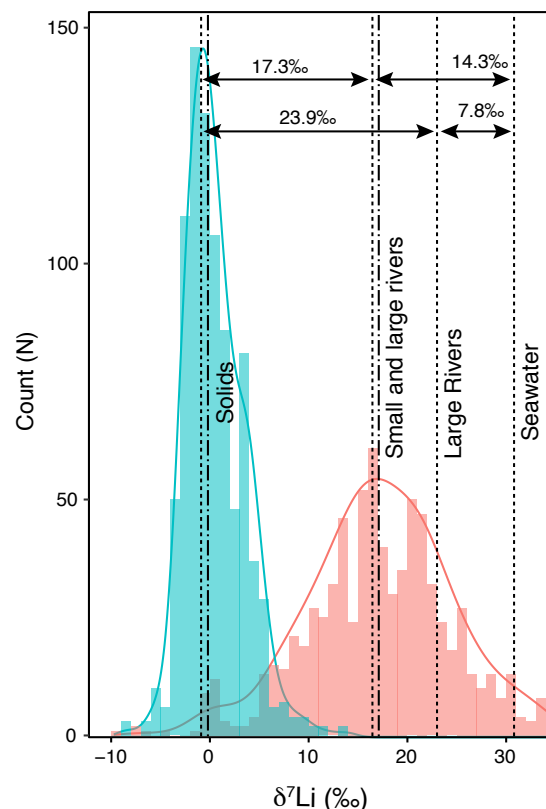
Figure 10: Histogram of a literature compilation of δ^7Li field data. Bin size is 1‰, and the density function for all the data is shown overlaid with a bandwidth of 1.5. Literature sources: Bagard et al. (2015); Clergue et al. (2015); Dellinger et al. (2014, 2015); Henchiri et al. (2016); Hindshaw et al. (2018); Huh et al. (1998, 2001); Kısakűrek et al. (2004, 2005); Lemarchand et al. (2010); Liu et al. (2013, 2015); Manaka et al. (2017); Millot et al. (2010a,c, 2011, 2012); Murphy et al. (2019); Négrel et al. (2010); Négrel et al. (2012); Pogge von Strandmann et al. (2006, 2010, 2014, 2017b); Pogge von Strandmann and Henderson (2015); Qiu et al. (2011); Ryu et al. (2014); Sauzéat et al. (2015); Teng et al. (2004); Tsai et al. (2014); Vigier et al. (2009); Wang et al. (2015); Weynell et al. (2017); Wimpenny et al. (2010b); Xiao et al. (2011). The 'Large Rivers' line is from Huh et al. (1998) and the seawater line is from Rosner et al. (2007). Dashed lines indicate the mode of the density functions whilst the dash-dot lines indcate the median values. The calculated differences are based on the dashed lines.

solid characterisation (including ^{7}Li-NMR) and DFT calculations offers a promising pathway to elucidate the factors controlling Li isotope fractionation into clay minerals: an essential pre-requisite for a quantitative understanding of the global Li geochemical cycle.

6. Acknowledgments

24

7. References

Bagard, M.-L., West, A. J., Newman, K., Basu, A. R., 2015. Lithium isotope fractionation in the Ganges-Brahmaputra floodplain and implications for groundwater imapct on seawater isotopic composition. Earth Planet. Sci. Lett. 432, 404–414.

Bigeleisen, J., 1965. Chemistry of isotopes. Science 147, 463–471.

Bogatko, S., Claeys, P., De Proft, F., Geerlings, P., 2013. Li$^+$ speciation and the use of ^{7}Li/^{6}Li isotope ratios for ancient climate monitoring. Chem. Geol. 357, 1–7.

Bohlin, M. S., Misra, S., Lloyd, N., Elderfield, H., Bickle, M. J., 2018. High-precision determination of lithium and magnesium isotopes utilising single column separation and multi-collector inductively coupled plasma mass spectrometry. Rapid Commun. Mass Spectrom. 32, 93–104.

Bouchez, J., von Blanckenburg, F., Schuessler, J. A., 2013. Modeling novel stable isotope ratios in the weathering zone. Am. J. Sci. 313, 267–308.

Brigatti, M. F., Lugli, C., Poppi, L., Foord, E. E., Kile, D. E., 2000. Crystal chemical variations in Li- and Fe-rich micas from Pikes Peak batholith (central Colorado). Am. Mineral. 85, 1275–1286.

Brindley, G. W., Bish, D. L., Wan, H.-M., 1977. The nature of kerolite, its relation to talc and stevensite. Miner. Mag. 41, 443–452.

Carignan, J., Cardinal, D., Eisenhauer, A., Galy, A., Rehkämper, M., Wombacher, F., Vigier, N., 2004. A reflection on Mg, Cd, Ca, Li and Si isotopic measurements and related reference materials. Geostand. Geoanal. Res. 28, 139–148.

Carignan, J., Vigier, N., Millot, R., 2007. Three secondary reference materials for lithium isotope measurements: Li7-N, Li6-N and LiCl-N solutions. Geostand. Geoanal. Res. 31, 7–12.

Carrado, K. A., Decarreau, A., Petit, S., Bergaya, F., Lagaly, G., 2006. Synthetic clay minerals and purification of natural clays. In: Bergaya, F., Theng, B. K. G., Lagaly, G. (Eds.), Handbook of Clay Science. Vol. 1 of Developments in Clay Science. Elsevier, Amsterdam, Ch. 4, pp. 115–139.

Chan, L.-H., Edmond, J. M., Thompson, G., 1993. A lithium isotope study of hot springs and metabasalts from mid-ocean ridge hydrothermal systems. J. Geophys. Res. 98, 9653–9659.

Chan, L.-H., Hein, J. R., 2007. Lithium contents and isotopic compositions of ferromanganese deposits from the global ocean. Deep-Sea Res. II 54, 1147–1162.

Clergue, C., Dellinger, M., Buss, H. L., Gaillardet, J., Benedetti, M. F., Dessert, C., 2015. Influence of atmospheric deposits and secondary minerals on Li isotopes budget in a highly weathered catchment, Guadeloupe (Lesser Antilles). Chem. Geol. 414, 28–41.

Decarreau, A., Vigier, N., Pálková, H., Petit, S., Vieillard, P., Fontaine, C., 2012. Partitioning of lithium between smectite and solution: An experimental approach. Geochim. Cosmochim. Acta 85, 314–325.

Dekov, V. M., Cuadros, J., Shanks, W. C., Koski, R. A., 2008. Deposition of talc – kerolite-smectite – smectite at seafloor hydrothermal vent fields: Evidence from mineralogical, geochemical and oxygen isotope studies. Chem. Geol. 247, 171–194.

Dellinger, M., Gaillardet, J., Bouchez, J., Calmels, D., Galy, V., Hilton, R. G., Louvat, P., France-Lanord, C., 2014. Lithium isotopes in large rivers reveal the cannibalistic nature of modern continental weathering and erosion. Earth Planet. Sci. Lett. 401, 359–372.

Dellinger, M., Gaillardet, J., Bouchez, J., Calmels, D., Louvat, P., Dosseto, A., Gorge, C., Alanoca, L., Maurice, L., 2015. Riverine Li isotope fractionation in the Amazon River basin controlled by the weathering regimes. Geochim. Cosmochim. Acta 164, 71–93.

Dessert, C., Dupré, B., François, L. M., Schott, J., Gaillardet, J., Chakrapani, G., Bajpai, S., 2001. Erosion of Deccan Traps determined by river geochemistry: impact on the global climate and the ^{87}Sr/^{86}Sr ratio of seawater. Earth Planet. Sci. Lett. 188, 459–474.

Dupuis, R., Benoit, M., Tuckerman, M. E., Méheut, M., 2017. Importance of a fully anharmonic treatment of equilibrium isotope fractionation properties of dissolved ionic species as evidenced by Li$^+$(aq). Acc. Chem. Res. 50, 1597–1605.

Eberl, D. D., Jones, B. F., Khoury, H. N., 1982. Mixed-layer kerolite/stevensite from the Amargosa Desert, Nevada. Clay Clay Miner. 30, 321–326.

Farmer, V. C., 1974. The layer silicates. In: The Infrared Spectra of Minerals. Vol. 4. Mineralogical Society, London, pp. 331–363.

Froelich, F., Misra, S., 2014. Was the late Paleocene-early Eocene hot because the Earth was flat? An ocean lithium isotope view of mountain building, continental weathering, carbon dioxide, and Earth's Cenozoic climate. Oceanography 27, 36–49.

Gíslason, S. R., Arnórsson, S., Ármannsson, H., 1996. Chemical weathering of basalt in southwest Iceland: Effects of runoff, age of rocks and vegetative/glacial cover. Am. J. Sci. 296, 837–907.

Greathouse, J., Sposito, G., 1998. Monte Carlo and molecular dynamics studies of interlayer structure in $Li(H_2O)_3$–smectites. J. Phys. Chem. B 102, 2406–2414.

Guggenheim, S., 2016. Introduction to Mg-rich clay minerals: Structure and composition. In: Pozo, M., Galán, E. (Eds.), Magnesian clays: Characterization, origins and applications. No. 2 in AIPEA Educational Series. AIPEA, Bari, Italy, pp. 1–62.

Güven, N., Carney, L. L., 1979. The hydrothermal transformation of sepiolite to stevensite and the effect of added chlorides and hydroxides. Clay Clay Miner. 27, 253–260.

Hall, J. M., Chan, L.-H., McDonough, W. F., Turekian, K. K., 2005. Determination of the lithium isotopic composition of planktic foraminifera and its application as a paleo-seawater proxy. Marine Geology 217, 255–265.

Harder, H., 1972. The role of magnesium in the formation of smectite minerals. Chem. Geol. 10, 31–39.

Hathorne, E. C., James, R. H., 2006. Temporal record of lithium in seawater: A tracer for silicate weathering? Earth Planet. Sci. Lett. 246, 393–406.

Henchiri, S., Gaillardet, J., Dellinger, M., Bouchez, J., Spencer, R. G. M., 2016. Riverine dissolved lithium isotopic signatures in low-relief central Africa and their link to weathering regimes. Geophys. Res. Lett. 43, 4391–4399.

Hindshaw, R. S., Aciego, S. M., Tipper, E. T., 2018. Li and U isotopes as a potential tool for monitoring active layer deepening in permafrost dominated catchments. Front. Earth Sci. 6, 102.

Hindshaw, R. S., Rickli, J., Leuthold, J., Wadham, J., Bourdon, B., 2014. Identifying weathering sources and processes in an outlet glacier of the Greenland Ice Sheet using Ca and Sr isotope ratios. Geochim. Cosmochim. Acta 145, 50–71.

Hochella, Jr, M. F., Banfield, J. F., 1995. Chemical weathering of silicates in nature: A microscopic perspective with theoretical considerations. In: White, A. F., Brantley, S. L., Ribbe, P. H. (Eds.), Chemical weathering rates of silicate minerals. Vol. 31 of Reviews in Mineralogy and Geochemistry. Mineralogical Society of America, Washington, DC, Ch. 8, pp. 353–406.

Huh, Y., Chan, L.-H., Edmond, J. M., 2001. Lithium isotopes as a probe of weathering processes: Orinoco river. Earth Planet. Sci. Lett. 194, 189–199.

Huh, Y., Chan, L.-H., Zhang, L., Edmond, J. M., 1998. Lithium and its isotopes in major world rivers: Implications for weathering and the oceanic budget. Geochim. Cosmochim. Acta 62, 2039–2051.

Jones, B. F., 1986. Clay mineral diagenesis in lacustrine sediments. In: Mumpton, F. A. (Ed.), Studies in diagenesis. Vol. 1578. U.S. Geological Survey, Washington, DC, pp. 291–300.

Kalo, H., Milius, W., Breu, J., 2012. Single crystal structure refinement of one- and two-layer hydrates of sodium fluorohectorite. RSC Adv. 2, 8452–8459.

Kısakűrek, B., James, R. H., Harris, N. B. W., 2005. Li and δ^7Li in Himalayan rivers: Proxies for silicate weathering? Earth Planet. Sci. Lett. 237, 387–401.

Kısakűrek, B., Widdowson, M., James, R. H., 2004. Behaviour of Li isotopes during continental weathering: the Bidar laterite profile, India. Chem. Geol. 212, 27–44.

Laurora, A., Brigatti, M. F., Malferrari, D., Galli, E., Rossi, A., 2011. The crystal chemistry of lizardite-1T from northern Apennines ophiolites near Modena, Italy. The Canad. Mineral. 49, 1045–1054.

Lechler, M., Pogge von Strandmann, P. A. E., Jenkyns, H. C., Prosser, G., Parente, M., 2015. Lithium-isotope evidence for enhanced silicate weathering during OAE 1a (Early Aptian Selli event). Earth Planet. Sci. Lett. 432, 210–222.

Lemarchand, E., Chabaux, F., Vigier, N., Millot, R., Pierret, M.-C., 2010. Lithium isotope systematics in a forested granitic catchment (Strengbach, Vosges Mountains, France). Geochim. Cosmochim. Acta 74, 4612–4628.

Li, G., West, A. J., 2014. Evolution of Cenozoic seawater lithium isotopes: Coupling of global denudation regime and shifting seawater sinks. Earth Planet. Sci. Lett. 401, 284–293.

Li, W., Beard, B. L., Li, C., Johnson, C. M., 2014. Magnesium isotope fractionation between brucite [$Mg(OH)_2$] and Mg aqueous species: Implications for silicate weathering and biogeochemical processes. Earth Planet. Sci. Lett. 394, 82–93.

Liu, X.-M., Rudnick, R. L., McDonough, W. F., Cummings, M. L., 2013. Influence of chemical weathering on the composition of the continental crust: Insights from Li and Nd isotopes in bauxite profiles developed on Columbia River Basalts. Geochim. Cosmochim. Acta 115, 73–91.

Liu, X.-M., Wanner, C., Rudnick, R. L., McDonough, W. F., 2015. Processes controlling δ^7Li in rivers illuminated by study of streams and groundwaters draining basalts. Earth Planet. Sci. Lett. 409, 212–224.

Lynton, S. J., Walker, R. J., Candela, P. A., 2005. Lithium isotopes in the system Qz-Ms-fluid: An experimental study. Geochim. Cosmochim. Acta 69, 3337–3347.

Mähler, J., Persson, I., 2012. A study of the hydration of the alkali metal ions in aqueous solution. Inorg. Chem. 51, 425–438.

Manaka, T., Araoka, D., Yoshimura, T., Hossain, H. M. Z., Nishio, Y., Suzuki, A., Kawahata, H., 2017. Downstream and seasonal changes of lithium isotope ratios in the Ganges-Brahmaputra river system. Geochem. Geophys. Geosys. 18, 3003–3015.

Martin de Vidales, J. L., Pozo, M., Alia, J. M., Garcia-Navarro, F., Rull, F., 1991. Kerolite-stevensite mixed-layers from the Madrid Basin, Central Spain. Clay Miner. 26, 329–342.

Meunier, A., 2005. Clays. Springer-Verlag, Berlin.

Michalski, J. R., Cuadros, J., Bishop, J. L., Dyar, M. D., Dekov, V., Fiore, S., 2015. Constraints on the crystal-chemistry of Fe/Mg-rich smectitic clays on Mars and links to global alteration trends. Earth Planet. Sci. Lett. 427, 215–225.

Millot, R., Guerrot, C., Innocent, C., Négrel, P., Sanjuan, B., 2011. Chemical, multi-isotopic (Li–B–Sr–U–H–O) and thermal characterization of Triassic formation waters from the Paris Basin. Chem. Geol. 283, 226–241.

Millot, R., Hegan, A., Négrel, P., 2012. Geothermal waters from the Taupo Volcanic Zone, New Zealand: Li, B and Sr isotopes characterization. Appl. Geochem. 27, 677–688.

Millot, R., Petelet-Giraud, E., Guerrot, C., Négrel, P., 2010a. Multi-isotopic composition (δ^7Li–δ^{11}B–δD–δ^{18}O) of rainwaters in France: Origin and spatio-temporal characterization. Appl. Geochem. 25, 1510–1524.

Millot, R., Scaillet, B., Sanjuan, B., 2010b. Lithium isotopes in island arc geothermal systems: Guadeloupe, Martinique (French West Indies) and experimental approach. Geochim. Cosmochim. Acta 74, 1852–1871.

Millot, R., Vigier, N., Gaillardet, J., 2010c. Behaviour of lithium and its isotopes during weathering in the Mackenzie Basin, Canada. Geochim. Cosmochim. Acta 74, 3897–3912.

Misra, S., Froelich, P. N., 2012. Lithium isotope history of Cenozoic seawater: changes in silicate weathering and reverse weathering. Science 335, 818–823.

Murphy, M. J., Porcelli, D., Pogge von Strandmann, P. A. E., Hirst, C. A., Kutscher, L., Katchinoff, J. A., Mörth, C.-M., Maximov, T., Andersson, P. S., 2019. Tracing silicate weathering processes in the permafrost-dominated Lena River watershed using lithium isotopes. Geochim. Cosmochim. Acta 245, 154–171.

Négrel, P., Millot, R., Brenot, A., Bertin, C., 2010. Lithium isotopes as tracers of groundwater circulation in a peat land. Chem. Geol. 276, 119–127.

Négrel, P., Millot, R., Guerrot, C., Petelet-Giraud, E., Brenot, A., Malcuit, E., 2012. Heterogeneities and interconnections in groundwaters: Coupled B, Li and stable-isotope variations in a large aquifer system (Eocene Sand aquifer, Southwestern France). Chem. Geol. 296-297, 83–95.

Nielsen, L. C., DePaolo, D. J., De Yoreo, J. J., 2012. Self-consistent ion-by-ion growth model for kinetic isotopic fractionation during calcite precipitation. Geochim. Cosmochim. Acta 86, 166–181.

Perdikatsis, B., Burzlaff, H., 1981. Strukturverfeinerung am Talk $Mg_3[(OH)_2Si_4O_{10}]$. Z. Kristall. 156, 177–186.

Phan, T. T., Capo, R. C., Stewart, B. W., Macpherson, G. L., Rowan, E. L., Hammack, R. W., 2016. Factors controlling Li concentration and isotopic composition in formation waters and host rocks of Marcellus Shale, Appalachian Basin. Chem. Geol. 420, 162–179.

Pistiner, J. S., Henderson, G. M., 2003. Lithium-isotope fractionation during continental weathering processes. Earth Planet. Sci. Lett. 214, 327–339.

Pogge von Strandmann, P. A. E., Burton, K. W., James, R. H., van Calsteren, P., Gíslason, S. R., 2010. Assessing the role of climate on uranium and lithium isotope behaviour in rivers draining a basaltic terrain. Chem. Geol. 270, 227–239.

Pogge von Strandmann, P. A. E., Burton, K. W., James, R. H., van Calsteren, P., Gíslason, S. R., Mokadem, F., 2006. Riverine behaviour of uranium and lithium isotopes in an actively glaciated basaltic terrain. Earth Planet. Sci. Lett. 251, 134–147.

Pogge von Strandmann, P. A. E., Desrochers, A., Murphy, M. J., Finlay, A. J., Selby, D., Lenton, T. M., 2017a. Global climate stabilisation by chemical weathering during the Hirnantian glaciation. Geochem. Persp. Let. 3, 230–237.

27

Pogge von Strandmann, P. A. E., Frings, P. J., Murphy, M. J., 2017b. Lithium isotope behaviour during weathering in the Ganges Alluvial Plain. Geochim. Cosmochim. Acta 198, 17–31.

Pogge von Strandmann, P. A. E., Henderson, G. M., 2015. The Li isotope response to mountain uplift. Geology 43, 67–70.

Pogge von Strandmann, P. A. E., Jenkyns, H. C., Woodfine, R. G., 2013. Lithium isotope evidence for enhanced weathering during Ocean Anoxic Event 2. Nat. Geosci. 6, 668–672.

Pogge von Strandmann, P. A. E., Porcelli, D., James, R. H., van Calsteren, P., Schaefer, B., Cartwright, I., Reynolds, B. C., Burton, K. W., 2014. Chemical weathering processes in the Great Artesian Basin: Evidence from lithium and silicon isotopes. Earth Planet. Sci. Lett. 406, 24–36.

Pokrovsky, O. S., Schott, J., Kudryavtzev, D. I., Dupré, B., 2005. Basalt weathering in Central Siberia under permafrost conditions. Geochim. Cosmochim. Acta 69, 5659–5680.

Qiu, L., Rudnick, R. L., McDonough, W. F., Bea, F., 2011. The behavior of lithium in amphibolite- to granulite-facies rocks of the Ivrea–Verbano Zone, NW Italy. Chem. Geol. 289, 76–85.

Reimers, C. E., Ruttenberg, K. C., Canfield, D. E., Christiansen, M. B., Martin, J. B., 1996. Porewater pH and authigenic phases formed in the uppermost sediments of the Santa Barbara Basin. Geochim. Cosmochim. Acta 60, 4037–4057.

Roberts, J., Kaczmarek, K., Langer, G., Skinner, L. C., Bijma, J., Bradbury, H., Turchyn, A. V., Lamy, F., Misra, S., 2018. Lithium isotopic composition of benthic foraminifera: A new proxy for paleo-pH reconstruction. Geochim. Cosmochim. Acta 236, 336–350.

Rosner, M., Ball, L., Peucker-Ehrenbrink, B., Blusztajn, J., Bach, W., Erzinger, J., 2007. A simplified, accurate and fast method for lithium isotope analysis of rocks and fluids, and δ^7Li values of seawater and rock reference materials. Geostand. Geoanal. Res. 31, 77–88.

Rudolph, W., Brooker, M. H., Pye, C. C., 1995. Hydration of lithium ion in aqueous solution. J. Phys. Chem. 99, 3793–3797.

Russell, J. D., Fraser, A. R., 1994. Infrared methods. In: Wilson, M. J. (Ed.), Clay mineralogy: Spectroscopic and chemical determinative methods. Vol. 23. Chapman & Hall, London, pp. 11–67.

Ryu, J.-S., Vigier, N., Lee, S.-W., Lee, K.-S., Chadwick, O. A., 2014. Variation of lithium isotope geochemistry during basalt weathering and secondary mineral transformations in Hawaii. Geochim. Cosmochim. Acta 145, 103–115.

Sauzéat, L., Rudnick, R. L., Chauvel, C., Garçon, M., Tang, M., 2015. New perspectives on the Li isotopic composition of the upper continental crust and its weathering signature. Earth Planet. Sci. Lett. 428, 181–192.

Schauble, E. A., 2004. Applying stable isotope fractionation theory to new systems. In: Johnson, C. M., Beard, B. L., Albarède, F. (Eds.), Geochemistry of Non-traditional Stable Isotopes. Vol. 55 of Reviews in Mineralogy & Geochemistry. Mineralogical Society of America, Washington, DC, pp. 65–111.

Steudel, A., Friedrich, F., Schuhmann, R., Ruf, F., Sohling, U., Emmerich, K., 2017. Characterization of a fine-grained interstratification of turbostatic talc and saponite. Minerals 7, 5.

Stoessell, R. K., Hay, R. L., 1978. The geochemical origin of sepiolite and kerolite at Amboseli, Kenya. Contrib. Mineral. Petrol. 65, 255–267.

Stumm, W., Morgan, J. J., 1996. Aquatic Chemistry: chemical equilibria and rates in natural waters, 3rd Edition. Wiley, New York, NY.

Tang, J., Dietzel, M., Böhm, F., Köhler, S. J., Eisenhauer, A., 2008. Sr^{2+}/Ca^{2+} and $^{44}Ca/^{40}Ca$ fractionation during inorganic calcite formation: II. Ca isotopes. Geochim. Cosmochim. Acta 72, 3733–3745.

Tardy, Y., Krempp, G., Trauth, N., 1972. Le lithium dans les minéraux argileux des sédiments et des sols. Geochim. Cosmochim. Acta 36, 397–412.

Taylor, T. I., Urey, H. C., 1938. Fractionation of the lithium and potassium isotopes by chemical exchange with zeolites. J. Chem. Phys. 6, 429–438.

Teng, F.-Z., McDonough, W. F., Rudnick, R. L., Dalpé, C., Tomascak, P. B., Chappell, B. W., Gao, S., 2004. Lithium isotopic composition and concentration of the upper continental crust. Geochim. Cosmochim. Acta 68, 4167–4178.

Theng, B. K. G., Hayashi, S., Soma, M., Seyama, H., 1997. Nuclear magnetic resonance and X-ray photoelectron spectroscopic investigation of lithium migration in montmorillonite. Clay. Clay Miner. 45, 718–723.

Tipper, E. T., Lemarchand, E., Hindshaw, R. S., Reynolds, B. C., Bourdon, B., 2012. Seasonal sensitivity of weathering processes: Hints from magnesium isotopes in a glacial stream. Chem. Geol. 312-313, 80–92.

Tomascak, P. B., 2004. Developments in the understanding and application of lithium isotopes in the Earth and planetary sciences. In: Johnson, C. M., Beard, B. L., Albarède, F. (Eds.), Geochemistry of Non-traditional Stable Isotopes. Vol. 55 of Reviews in Mineralogy & Geochemistry.

Mineralogical Society of America, Washington, DC, pp. 153–195.

Tosca, N., Masterson, A. L., 2014. Chemical controls on incipient Mg-silicate crystallization at 25°C: Implications for early and late diagenesis. Clay Miner. 49, 195–224.

Tosca, N. J., 2016. Geochemical pathways to Mg-silicate formation. In: Pozo, M., Gálan, E. (Eds.), Magnesian clays: Characterization, origins and applications. No. 2 in AIPEA Educational Series. AIPEA, Bari, Italy, pp. 283–330.

Tsai, P.-H., You, C.-F., Huang, K.-F., Chung, C.-H., Sun, Y.-B., 2014. Lithium distribution and isotopic fractionation during chemical weathering and soil formation in a loess profile. J. Asian Earth Sci. 87, 1–10.

Tutolo, B. M., Tosca, N. J., 2018. Experimental examination of the Mg-silicate-carbonate system at ambient temperature: Implications for alkaline chemical sedimentation and lacustrine carbonate formation. Geochim. Cosmochim. Acta 225, 80–101.

Verney-Carron, A., Vigier, N., Millot, R., 2011. Experimental determination of the role of diffusion on Li isotope fractionation during basaltic glass weathering. Geochim. Cosmochim. Acta 75, 3452–3468.

Vigier, N., Decarreau, A., Millot, R., Carignan, J., Petit, S., France-Lanord, C., 2008. Quantifying Li isotope fractionation during smectite formation and implications for the Li cycle. Geochim. Cosmochim. Acta 72, 780–792.

Vigier, N., Gislason, S. R., Burton, K. W., Millot, R., Mokadem, F., 2009. The relationship between riverine lithium isotope composition and silicate weathering rates in Iceland. Earth Planet. Sci. Lett. 287, 434–441.

Vigier, N., Goddéris, Y., 2015. A new approach for modeling Cenozoic ocean lithium isotope paleo-variations: the key role of climate. Clim. Past. 11, 635–645.

Vogels, R. J. M. J., Kloprogge, J. T., Geus, J. W., 2005. Synthesis and characterization of saponite clays. Am. Mineral. 90, 931–944.

Von Damm, K. L., Edmond, J. M., 1984. Reverse weathering in the closed-basin lakes of the Ethiopian Rift. Am. J. Sci. 284, 835–862.

Wang, Q.-L., Chetelat, B., Zhao, Z.-Q., Ding, H., Li, S.-L., Wang, B.-L., Li, J., Liu, X.-L., 2015. Behavior of lithium isotopes in the Changjiang River system: Sources effects and response to weathering and erosion. Geochim. Cosmochim. Acta 151, 117–132.

Wang, W., Qin, T., Zhou, C., Huang, S., Wu, Z., Huang, F., 2017a. Concentration effect on equilibrium fractionation of Mg-Ca isotopes in carbonate minerals: Insights from first-principles calculations. Geochim. Cosmochim. Acta 208, 185–197.

Wang, W., Zhou, C., Qin, T., Kang, J.-T., Huang, S., Wu, Z., Huang, F., 2017b. Effect of Ca content on equilbrium Ca isotope fractionation between orthopyroxene and clinopyroxene. Geochim. Cosmochim. Acta 219, 44–56.

Wanner, C., Sonnenthal, E. L., Liu, X.-M., 2014. Seawater δ^7Li: A direct proxy for global CO_2 consumption by continental silicate weathering? Chem. Geol. 381, 154–167.

Weynell, M., Wiechert, U., Schuessler, J. A., 2017. Lithium isotopes and implications on chemical weathering in the catchment of Lake Donggi Cona, northeastern Tibetan Plateau. Geochim. Cosmochim. Acta 213, 155–177.

Wilkins, R. W. T., Ito, J., 1967. Infrared spectra of some synthetic talcs. Am. Mineral. 52, 1649–1661.

Williams, L. B., Hervig, R. L., 2005. Lithium and boron isotopes in illite-smectite: the importance of crystal size. Geochim. Cosmochim. Acta 69, 5705–5716.

Wimpenny, J., Colla, C. A., Yu, P., Yin, Q.-Z., Rustad, J. R., Casey, W. H., 2015. Lithium isotope fractionation during uptake by gibbsite. Geochim. Cosmochim. Acta 168, 133–150.

Wimpenny, J., Gíslason, S. R., James, R. H., Gannoun, A., Pogge von Strandmann, P. A. E., Burton, K. W., 2010a. The behaviour of Li and Mg isotopes during primary phase dissolution and secondary mineral formation in basalt. Geochim. Cosmochim. Acta 74, 5259–5279.

Wimpenny, J., James, R. H., Burton, K. W., Gannoun, A., Mokadem, F., Gíslason, S. R., 2010b. Glacial effects on weathering processes: New insights from the elemental and lithium isotopic composition of West Greenland rivers. Earth Planet. Sci. Lett. 290, 427–437.

Wunder, B., Deschamps, F., Watenphul, A., Guillot, S., Meixner, A., Romer, R. L., Wirth, R., 2010. The effect of chrysotile nanotubes on the serpentine-fluid Li-isotopic fractionation. Contrib. Mineral. Petrol. 159, 781–790.

Wunder, B., Meixner, A., Romer, R. L., Feenstra, A., Schettler, G., Heinrich, W., 2007. Lithium isotope fractionation between Li-bearing staurolite, Li-mica and aqueous fluids: An experimental study. Chem. Geol. 238, 277–290.

Wunder, B., Meixner, A., Romer, R. L., Heinrich, W., 2006. Temperature-dependent isotopic fractionation of lithium between clinopyroxene and

high-pressure hydrous fluids. Contrib. Mineral. Petrol. 151, 112–120.

Wungu, T. D. K., Diño, W. A., Dipojono, H. K., Kasai, H., 2011. Effect of lithium absorption at tetrahedral site and isomorphic substitution on montmorillonite properties: A density functional theory study. Jap. J. Appl. Phys. 50, 055701.

Xiao, Y., Hoefs, J., Hou, Z., Simon, K., Zhang, Z., 2011. Fluid/rock interaction and mass transfer in continental subduction zones: constraints from trace elements and isotopes (Li, B, O, Sr, Nd, Pb) in UHP rocks from the Chinese Continental Scientific Drilling Program, Sulu, East China. Contrib. Mineral. Petrol. 162, 797–819.

Xu, Z., Stebbins, J. F., 1995. ^{6}Li nuclear magnetic resonance chemical shifts, coordination number and relaxation in crystalline and glassy silicates. Solid State Nucl. Magn. Reson. 5, 103–112.

Yamaji, K., Makita, Y., Watanabe, H., Sonoda, A., Kanoh, H., Hirotsu, T., Ooi, K., 2001. Theoretical estimation of lithium isotopic reduced partition function ratio for lithium ions in aqueous solution. J. Phys. Chem. A 105, 602–613.

Zhang, L., Chan, L.-H., Gieskes, J. M., 1998. Lithium isotope geochemistry of pore waters from Ocean Drilling Program Sites 918 and 919, Irminger Basin. Geochim. Cosmochim. Acta 62, 2437–2450.
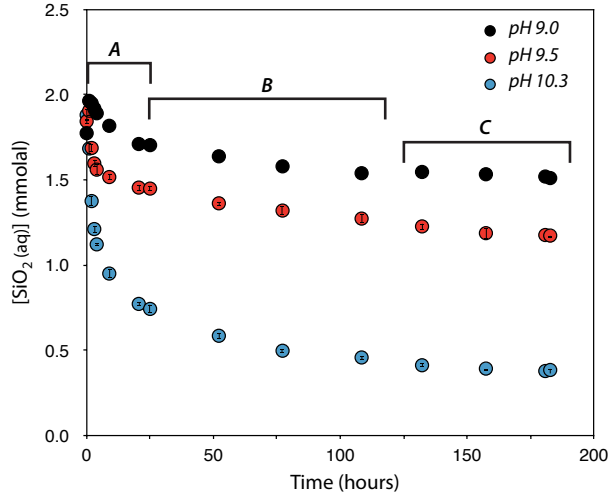
8. Supplementary Material

Figure S1: Evolution of SiO$_2$ concentrations in solution with time for additional experiments conducted with identical initial solution compositions to the '240417' series of experiments. Three phases are illustrated. **A** is a nucleation-dominated phase which lasts several hours and is characterised by rapid removal of constituents from solution. **B** is a growth-dominated phase which lasts several days and is characterised by slower removal of constituents from solution, reflecting growth of newly precipitated nuclei. **C** is steady-state behaviour where the element concentrations no longer change within experimental error.

8.1. Monte Carlo minimum misfit method

The "total" δ^7Li of each sample, be it a bulk, residue or exchange solution sample is given by the mass weighted sum of δ^7Li associated with each bonding environment (octahedral, pseudo-hexagonal and outer-sphere) as identified by ^{7}Li-NMR. Given the difference between the exchange solution data and the residue data there are at least two different δ^7Li values corresponding to individual bonding environments. Since the mass fraction of Li in each environment is constrained by ^{7}Li-NMR, it is possible to write down a mass balance equation for each sample:

$$\delta^7 Li_{total} = f_{oct} \cdot \delta^7 Li_{oct} + f_{ph} \cdot \delta^7 Li_{ph} + f_{os} \cdot \delta^7 Li_{os} \tag{1}$$

where the subscripts *oct*, *ph* and *os* refer to the octahedral, pseudo-hexagonal and outer-sphere environments respectively and f is the mass fraction in each environment.

Since δ^7Li$_{total}$ and the mass fractions were determined for six samples (bulk, residue and exchange) and there are three unknowns in this equation, δ^7Li$_{oct}$, δ^7Li$_{ph}$ and δ^7Li$_{os}$, the problem is over determined and it is possible to solve for each of the unknowns. This was done using a misfit approach where the misfit is a measure of the difference between the measured and calculated δ^7Li of the sample:

$$misfit = \sqrt{\sum_k \left(\delta^7 Li_{total-measured} - f_{oct} \cdot \delta^7 Li_{oct} - f_{ph} \cdot \delta^7 Li_{ph} - f_{os} \cdot \delta^7 Li_{os} \right)^2} \tag{2}$$

31

where k is the number of samples (six), the fractions are determined from ^{7}Li-NMR spectra and δ^7Li_{oct}, δ^7Li_{ph}, δ^7Li_{os} are variables, allowed to vary over a plausible range of parameter space.

The minimum misfit was found as a unique minimum corresponding to optimum (or best fit) values of δ^7Li_{oct}, δ^7Li_{ph} and δ^7Li_{os}. The uncertainty on these values was determined by using a Monte-Carlo approach, creating 10000 synthetic data sets using a gaussian distribution of errors based on the uncertainties associated with apportioning the mass fractions in each crystallographic site and the measurement uncertainties of δ^7Li on the Neptune.

The minimisation has been represented visually by plotting the mean of the misfit generated by the Monte-Carlo simulation over an appropriate range of parameter space (Fig. S2). The misfit is represented by the colour gradient and the contours. Since there are three variables, a 2D representation has been given by plotting a slice in the δ^7Li_{oct}, δ^7Li_{ph} and δ^7Li_{os} parameter space at the best fit value in the third dimension. Note that whilst a single solution has been determined, the optimum δ^7Li_{ph} value shows a broad dependency in particular on δ^7Li_{os} value which is why the uncertainty is large, whereas the δ^7Li_{oct} and δ^7Li_{os} values are relatively well constrained.

Finally, a visual check on the quality of these calculated fractionation factors is given by plotting the modelled vs the measured δ^7Li_{total} (Fig. 8a). The data scatter very closely around the 1:1 line indicating the robustness of the fit.
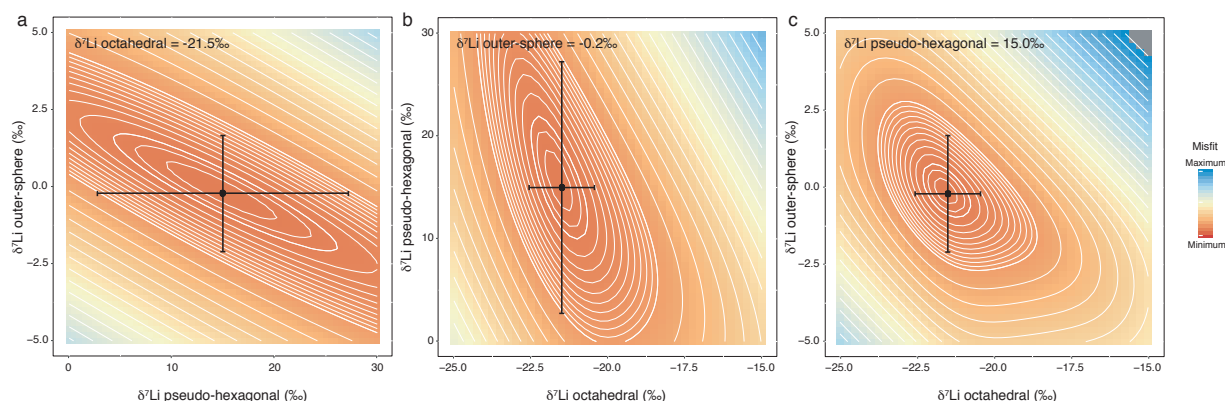

Figure S2: Contour maps indicating the misfit between measured δ^7Li values and calculated values when varying two of the fractionation factors. The third fractionation factor is held constant at its optimum value for the purposes of plotting. The black points indicate the optimum (smallest misfit) values for the two fractionation factors plotted and 1 sigma error bars are also shown.